

The Gravitational Wave Universe Toolbox:

A software package to simulate observation of the Gravitational Wave Universe with different detectors

Shu-Xu Yi^{1,5*}, Gijs Nelemans^{1,2,3}, Christiaan Brinkerink¹, Zuzanna Kostrzewa-Rutkowska^{4,1,2}, Sjoerd T. Timmer¹,
Fiorenzo Stoppa¹, Elena M. Rossi⁴, and Simon F. Portegies Zwart⁴

¹ Department of Astrophysics/IMAPP, Radboud University, P O Box 9010, NL-6500 GL Nijmegen, The Netherlands

² SRON, Netherlands Institute for Space Research, Sorbonnelaan 2, NL-3584 CA Utrecht, The Netherlands

³ Institute of Astronomy, KU Leuven, Celestijnenlaan 200D, B-3001 Leuven, Belgium

⁴ Leiden Observatory, Leiden University, PO Box 9513, NL-2300 RA Leiden, the Netherlands

⁵ Key Laboratory of Particle Astrophysics, Institute of High Energy Physics, Chinese Academy of Sciences, 19B Yuquan Road, Beijing 100049, People's Republic of China

ABSTRACT

Context. As the importance of Gravitational Wave (GW) astrophysics increases rapidly, astronomers interested in GW who are not experts can have the need to get a quick idea of what GW sources can be detected by certain detectors and the accuracy of the measured parameters.

Aims. The GW-Toolbox is a set of easy-to-use, flexible tools to simulate observations on the GW universe with different detectors, including ground-based interferometers (advanced LIGO, advanced VIRGO, KAGRA, Einstein Telescope, Cosmic Explorer and also customised interferometers), space-borne interferometers (LISA and a customised design), pulsar timing arrays mimicking the current working ones (EPTA, PPTA, NANOGrav, IPTA) and future ones. We include a broad range of sources such as mergers of stellar mass compact objects, namely black holes, neutron stars and black hole-neutron stars, supermassive black hole binaries mergers and inspirals, Galactic double white dwarfs in ultra-compact orbit, extreme mass ratio inspirals and Stochastic GW backgrounds.

Methods. We collect methods to simulate source populations and determine their detectability with various detectors. The paper aims at giving a comprehensive description of the methodology and functionality of the GW-Toolbox.

Results. The GW-Toolbox produces results that are consistent with previous work in literature, and the tools can be accessed with a website interface (gw-universe.org) or as a python package (<https://bitbucket.org/radboudradiolab/gwtoolbox>). In the future, it will be upgraded with more functions.

Key words. Gravitational waves, stars:neutron, stars:black holes, stars:white dwarfs, methods:numerical, galaxies:evolution, large-scale structure of the Universe

1. Introduction

Gravitational Wave (GW) astrophysics rises quickly into a pivotal branch of astronomy. A growing number of researchers from different fields find GW interesting and relevant to their various scientific goals (e.g. [Petiteau et al. 2013](#); [Lasky et al. 2016](#); [Caprini & Figueroa 2018](#); [Nelemans 2018](#); [McWilliams et al. 2019](#); [Barausse et al. 2020](#)). The first opened frequency window covers $\sim 10 - 1000$ Hz (a.k.a., the kHz band), which corresponds to the working frequency range of ground-based interferometers, e.g., the operating 2nd generation detectors advanced Laser Interferometer Gravitational-Wave Observatory (LIGO)/Virgo interferometer (Virgo)/Kamioka Gravitational Wave Detector (KAGRA) ([Harry & LIGO Scientific Collaboration 2010](#); [Acernese et al. 2015](#); [Kagra Collaboration et al. 2019](#)) and the planned 3rd generation detectors e.g., Einstein Telescope (ET, [Punturo et al. 2010](#)) and Cosmic Explorer (CE, [Reitze et al. 2019](#)). Space-borne interferometers, e.g., Laser Interferometer Space Antenna (LISA, [Amaro-Seoane et al. 2017](#)) and other similar projects, e.g., DECIGO ([Kawamura et al. 2006](#)), Taiji ([Mei et al. 2020](#)) and Tianqin ([Luo et al. 2016](#)), will cover the GW spectrum in the

frequency range $\sim 10^{-3} - 1$ Hz (a.k.a., mHz band). At even lower frequencies, pulsar timing arrays (PTAs, [Hobbs & Dai e.g. 2017](#); [Dahal e.g. 2020](#)) are used to probe GWs with frequencies around $10^{-8} - 10^{-5}$ Hz (a.k.a., nHz band). There are also attempts to search for GW at frequencies higher than the kHz regime, i.e., MHz/GHz ([Aggarwal et al. 2020](#)). Although this frequency range is another important part of the GW Universe, which is full of opportunities to discovery new physics and phenomena, we do not include detectors and sources of this frequency range in the GW-Toolbox at this stage, due to its larger uncertainties.

Together, these detectors are sensitive to a very broad range of GW sources, where higher frequency detectors are sensitive to smaller objects. In the frequency range $\sim 10 - 1000$ Hz, there are inspiral and mergers of stellar mass compact object binaries, spinning neutron stars and supernovae explosions (see e.g., [Clark et al. 1979](#); [Thorne 1987](#); [Schutz 1989](#); [Lipunov et al. 1997](#); [Portegies Zwart & McMillan 2000](#); [Belczynski et al. 2002](#); [Ott 2009](#); [Goetz & Riles 2011](#); [Postnov & Yungelson 2014](#)). On the other hand, the early inspiral phase of stellar mass compact object binaries occupy the frequency range $\sim 10^{-3} - 1$ Hz ([Sesana 2016](#)). Also white dwarfs binaries, which are not compact enough to be detected by kHz detectors, are prominent sources for mHz

* sxyi@ihep.ac.cn

detectors (e.g., Nelemans et al. 2001; Ruiter et al. 2010; Sesana 2016; Lamberts et al. 2018; Tauris 2018; Sesana et al. 2020; Lau et al. 2020). Since BH sizes increase with mass, the mHz detectors are sensitive to mergers of supermassive BHs (SMBHs) $10^3 - 10^8 M_{\odot}$ (e.g., Sesana et al. 2005; Berti et al. 2006) and extreme mass ratio inspirals (EMRIs, see Gair et al. 2004; Amaro-Seoane et al. 2007). Again, in the early inspiral phase, SMBH binaries occupy the low frequency end of the spectrum $\sim 10^{-8} - 10^{-5}$ Hz, either as individual sources or as a stochastic background (Sazhin 1978; Detweiler 1979; Hellings & Downs 1983; Jenet et al. 2005; Sesana et al. 2008).

The first detection of GW was made by the LIGO/Virgo Collaboration (LVC) in 2015 (Abbott et al. 2016). The event GW150914 originates from the merger of a binary black hole (BBH) and already had interesting astrophysical implications (see Abbott et al. 2016; Belczynski et al. 2016). Since then, there have been 90 GW events detected (as reported by LVC Abbott et al. 2019b, 2020c, 2021b), and there are more candidates reported by other groups from the public strain data). These events include mergers of BBH, double neutron stars (DNS, e.g., GW170817 and GW190425) and Black Hole-Neutron stars (BHNS, e.g. GW190426, GW200105, GW200115 (Abbott et al. 2021a)). The population of detected BBH mergers provides important clues on stellar formation and evolution history (e.g., The LIGO Scientific Collaboration et al. 2020). Among the detected sources, there are several unique systems which provide input to and even challenge current stellar evolution theory (e.g., GW190412, GW190814) and provide insight into the nature of neutron star matter (GW170817, GW190425). The multi-messenger observations of the DNS merger event GW170817/GRB 170817A/AT 2017gfo brought huge progress on astrophysics, fundamental physics and cosmology (e.g. Abbott et al. 2017a,b,c,d,e,f; Coulter et al. 2017; Pian et al. 2017; Abbott et al. 2018b,a, 2019a,c,d, 2020a). Future detectors like ET will vastly increase the detection reach and thus allow even broader science investigations (e.g. Maggiore et al. 2020).

Also PTA observations are routinely happening, and although there has no conclusive evidence on GW detection with PTA¹, the communities are putting more and more stringent upper limits on the nHz GW signals (van Haasteren et al. 2011; Demorest et al. 2013; Lentati et al. 2015; Arzoumanian et al. 2018; Verbiest et al. 2016; Aggarwal et al. 2019, 2020) and already ruled out some theories of galaxy evolution (Shannon et al. 2013, 2015). Future studies, in particular including SKA will make significant steps in the science that can be done (e.g. Janssen et al. 2015).

In the following sections we describe the GW-Toolbox, while in section 5 we show the results and compare these to the literature. In sections 6 and 7 we discuss the caveats, further plans and summarize the paper.

2. The Gravitational Wave Universe Toolbox

The GW-Toolbox (website: gw-universe.org)² is a set of tools for a broad audience to quickly simulate the observation on the GW universe with different detectors. The results include the expected number of detections, synthetic catalogues and parameter uncertainties. We include three classes of GW detectors, namely

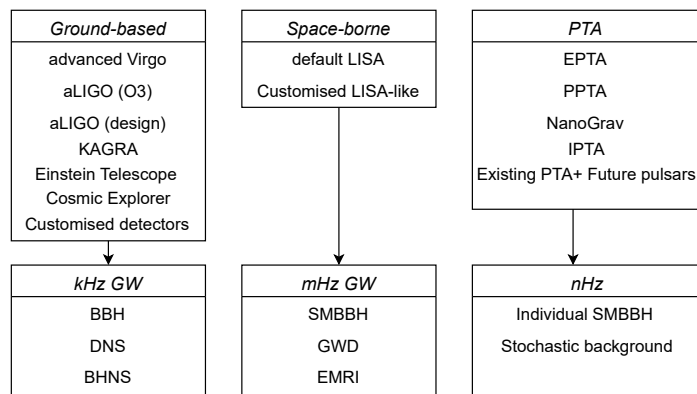


Fig. 1. A summary of detectors and sources included in the GW-Toolbox

Earth-based interferometers, space-borne interferometers, and PTAs. In each of these classes, the GW-Toolbox has the following detectors with default and customised settings:

- *Earth-based interferometers:*
 - Advanced LIGO in O3
 - Advanced LIGO at final design sensitivity
 - Advanced Virgo at final design sensitivity
 - KAGRA
 - Einstein telescope
 - Cosmic Explorer
 - A LIGO/Virgo-Like interferometer with customised parameters
- *Space-borne interferometers:*
 - default LISA
 - LISA-like spacecraft with customised parameters
- *Pulsar Timing Arrays:*
 - Existing EPTA
 - Existing PPTA
 - Existing NANOGrav
 - Existing IPTA
 - any of the existing PTAs plus simulated new pulsars to mimic future PTAs

The three classes of detectors correspond to the three main frequency regimes, namely kHz, mHz and nHz. In each of these regimes, we include the following sources.

- *kHz GW:*
 - Binary BH (BBH) mergers
 - Double Neutron Star (DNS) mergers
 - BH-Neutron Star (BHNS) mergers
- *mHz GW:*
 - Supermassive BH Binary Mergers (SMBBH)
 - Close Galactic White Dwarf binaries inspirals (GWD)
 - Extreme Mass Ratio Inspirals (EMRIs, Stellar mass BHs inspiraling into supermassive BHs)
- *nHz GW:*
 - Individual SMBBH inspiral
 - A stochastic GW background

See figure 1 for a summary of the detectors and sources. In practice, the logical flow of the GW-Toolbox is to first select the detector class and the detector parameters, then choose the source class, select its parameters and run. For some of the sources, the underlying cosmological model is also relevant to the simulation, where users are able to select a certain build-in cosmology or to

¹ NanoGrav found evidence for a common stochastic signal across pulsars, but there is no significant evidence of that being a GW (Arzoumanian et al. 2020).

² Python package repository: bitbucket.org/radboudradiolab/gwtoolbox.

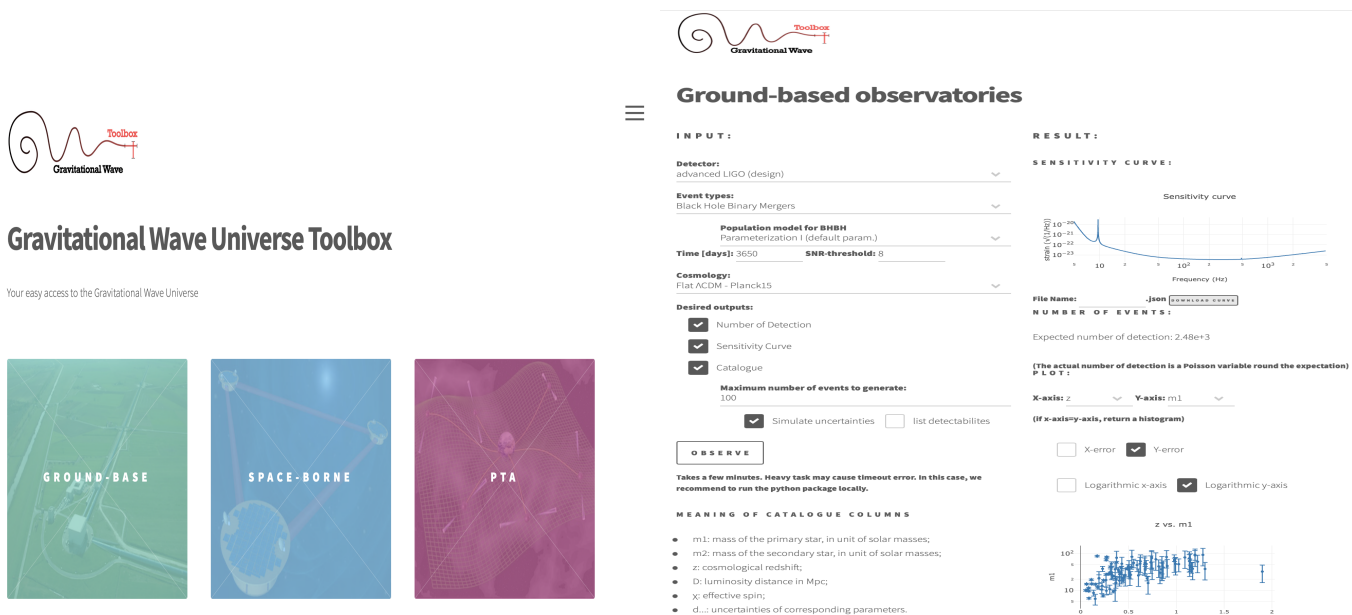


Fig. 2. Screen shot of the GWT start page (left) and ground-based observatories page with results for advanced LIGO (right).

input parameters for a self-defined Λ -CDM cosmological model. Examples in this paper are simulated with the cosmology model that corresponds to Planck DR15 (Planck Collaboration et al. 2016). We use the *astropy* package (Astropy Collaboration et al. 2013, 2018) with the cosmology model “Planck15”. Changing to more up-to-date “Planck18” cosmology model does not significantly change the simulation catalogues.

The results in general are the expected number of detections of the selected sources, and a synthetic catalogue with/without uncertainties on parameters. Plots and histograms of parameters of the catalogue can be made in-browser, and the figures and catalogue can also be exported. In figure 2, a screen shot of the GW-Toolbox website with the top-level selection is shown (left panel), in addition to an example of the kHz detector selection page (right panel).

This paper aims at giving a comprehensive description of the methodology and the functionality of the GW-Toolbox. The paper is organised with a similar structure as the set-up of the GW-Toolbox. For each class of sources, a model for the Universe is made in which the sources are distributed in space, time and other relevant parameters (such as mass, spins etc) according to a pre-defined population model. The user is allowed to change the population model, according to a parametrised formalism. In section 3, we give description on each of the population models.

The resulting GW source population is then simulated to be observed against a selected GW detector from the above list. After source and detector are determined, the *detected* sources are selected using a signal-to-noise ratio (SNR) criterion. Using the Fisher Matrix formalism, the uncertainties of parameters of the detected sources are estimated. In section 4, we describe how the response of the detector is represented, and the algorithm to generate the catalogue of detected sources. For PTAs, we describe our simplified representation of the pulsar array, the properties of the timing noises and the observation campaign.

3. Implementation 1: The Universe model

We first turn to the implementation of the Universe model, in which we select source population models from the literature and in some cases, allow users to change or adapt the source population. There are many reviews of GW sources that discuss these in more detail, such as Sathyaprakash & Schutz (2009); González et al. (2013) and below we discuss the relevant ones. We start with sources for ground-based detectors, where we concentrate on compact binary mergers detectable with ground-based detectors, and then move to space-borne detectors, with supermassive binary black hole mergers, white dwarf compact binaries and extreme mass-ratio inspirals (EMRIs) as sources, and finish with pulsar timing arrays for which we discuss individual supermassive black hole binaries as well as stochastic background.

3.1. Sources for Ground Based detectors

There have been many studies of the formation and population of sources for ground based detectors (e.g. Phinney 1991; Schneider et al. 2001; Fryer & Kalogera 2001; Belczynski et al. 2002; Dominik et al. 2015; de Mink & Belczynski 2015) and the population depends in a complicated way on many uncertain aspects of binary evolution, the formation of binary stars and even the metallicity evolution of the cosmic star formation history. We take a simple, yet flexible approach by using a parametrised description of the source populations (but see e.g. Moe & Di Stefano 2017; Chruslińska et al. 2019, 2020 for discussions of some of the complications).

3.1.1. Binary Black Hole Mergers

The population of BBH mergers is the most prominent in current GW detectors (Abbott et al. 2020c). The source population is characterised by the merger rate as a function of redshift and the distribution of masses and spins (e.g. Mapelli et al. 2017; Farr et al. 2011; Kovetz et al. 2017; Talbot & Thrane 2018; Postnov & Kuranov 2019; Abbott et al. 2019e).

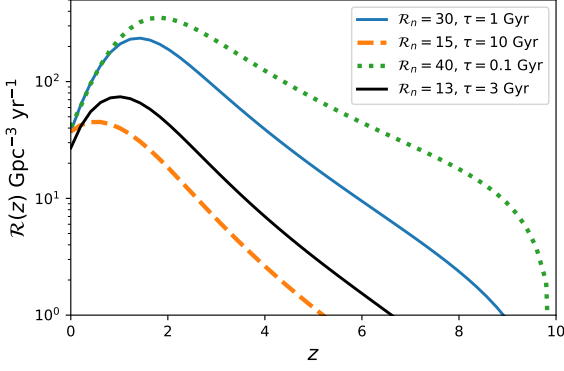


Fig. 3. $\mathcal{R}(z)$, [eq. (2)] with different \mathcal{R}_0 and τ .

In the population model for BBH, the merger rate density is expressed as:

$$\dot{n}(z, m_1, q, \chi) = \mathcal{R}(z)f(m_1)\pi(q)P(\chi), \quad (1)$$

where $f(m_1)$ is the mass function of the primary (heavier) black hole, $\pi(q)$ and $P(\chi)$ are the probability distributions of the mass ratio $q \equiv m_2/m_1$ and the effective spin χ respectively. \mathcal{R} as function of z is often refer to as the cosmic merger rate density. We take the parameterisation as in (Vitale et al. 2019):

$$\mathcal{R}(z_m) = \mathcal{R}_n \int_{z_m}^{\infty} \psi(z_f)P(z_m|z_f)dz_f, \quad (2)$$

where $\psi(z)$ is the Madau-Dickinson star formation rate:

$$\psi(z) = \frac{(1+z)^\alpha}{1 + \left(\frac{1+z}{C}\right)^\beta}, \quad (3)$$

with $\alpha = 2.7$, $\beta = 5.6$, $C = 2.9$ (Madau & Dickinson 2014), and $P(z_m|z_f, \tau)$ is the probability that the BBH merger at z_m if the binary is formed at z_f , which we refer to as the distribution of delay time with the form (Vitale et al. 2019):

$$P(z_m|z_f, \tau) = \frac{1}{\tau} \exp\left[-\frac{t_f(z_f) - t_m(z_m)}{\tau}\right] \frac{dt}{dz}. \quad (4)$$

In the above equation, t_f and t_m are the look back time corresponding to z_f and z_m respectively.

We give plots of $\mathcal{R}(z)$ with different \mathcal{R}_n and τ in figure 3. The default parameters are set to $\mathcal{R}_n = 13 \text{ Gpc}^{-3} \text{ yr}^{-1}$ and $\tau = 3 \text{ Gyrs}$, which are compatible with the local merger rate of BBH found in O3a (The LIGO Scientific Collaboration et al. 2020).

Although some information is known about the masses of the observed BBH (The LIGO Scientific Collaboration et al. 2020), we assume a generic mass function $p(m_1)$:

$$p(m_1) \propto \begin{cases} \exp\left(-\frac{c}{m_1 - \mu}\right)(m_1 - \mu)^{-\gamma}, & m_1 \leq m_{\text{cut}} \\ 0, & m_1 > m_{\text{cut}} \end{cases} \quad (5)$$

The distribution of $p(m_1)$ is defined for $m_1 > \mu$, which has a power law tail of index $-\gamma$ and a cut-off above m_{cut} . When $\gamma = 3/2$, the distribution becomes a shifted Lévy distribution. $p(m_1)$ peaks at $m_1 = c/\gamma + \mu$. We set $\mu = 3$, $\gamma = 2.5$, $c = 6$, $m_{\text{cut}} = 95 M_\odot$ as default, which result in simulated catalogue that fits

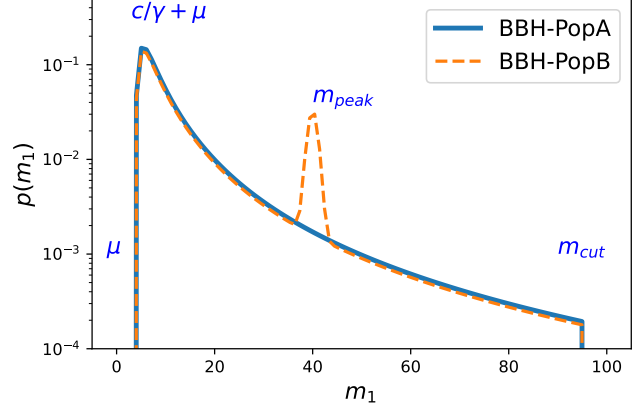


Fig. 4. The primary BH mass distribution in the default models of BBH-PopA/B, see eqns (5), (6). Here we mark μ , $\mu + c/\gamma$ and m_{peak} in the plot, to give an intuition of these quantities.

with the observed one (see section 5.1). The normalization of $p(m_1)$ is

$$c^{1-\gamma}\Gamma(\gamma - 1, \frac{c}{m_{\text{cut}} - \mu}),$$

where $\Gamma(a, b)$ is the upper incomplete gamma function;

In order to provide more flexibility, we also provide an alternative $p(m_1)$, which has an extra Gaussian peak component $p_{\text{peak}}(m_1)$ on top of that in equation (5):

$$p_{\text{peak}}(m_1) = A_{\text{peak}} \exp\left[-\left(\frac{m_1 - m_{\text{peak}}}{\sigma_{\text{peak}}}\right)^2\right], \quad (6)$$

the normalization of the alternative $p(m_1)$ is:

$$c^{1-\gamma}\Gamma(\gamma - 1, \frac{c}{m_{\text{cut}} - \mu}) + \sqrt{2\pi}\sigma_{\text{peak}}A_{\text{peak}}.$$

We denote the population model without/with the peak component in the mass function as BBH-PopA/B. Our default parameters for the peak component are $A_{\text{peak}} = 0.002$, $m_{\text{peak}} = 40 M_\odot$, $\sigma_{\text{peak}} = 1 M_\odot$, which are compatible with that implied from GWTC-3. In figure 4, we plot the mass distributions for BBH-PopA/B.

For $\pi(q)$ we use a uniform distribution between $[q_{\text{cut}}, 1]$ and assume χ follows a truncated Gaussian distribution centered at zero with standard deviation σ_χ , which is limited between -1 and 1 as demanded by general relativity. The actual mass ratio distribution is still poorly constrained from observation. The discovery of the GW190412 with asymmetric masses implies that the mass ratio distribution can be quite board (Abbott et al. 2020b). The Gaussian spin model is consistent with the finding in The LIGO Scientific Collaboration et al. (2020). The default parameters we use are $q_{\text{cut}} = 0.4$ and $\sigma_\chi = 0.1$. Those parameters in the population model can all be reset by users in both the web interface or in the python package.

3.1.2. Double neutron star mergers

For the population model of DNS mergers, the merger rate density is similarly expressed as:

$$\dot{n}(z, m_a, m_b, \chi) = \mathcal{R}(z)p(m_a)p(m_b)P(\chi), \quad (7)$$

where $\mathcal{R}(z)$ is taking the same form as in BBH population model, but with a different default setting: $\mathcal{R}_n = 300 \text{ Gpc}^{-3} \text{ yr}^{-1}$ and $\tau = 3 \text{ Gyrs}$, which are compatible with the local merger rate of DNS found with GWTC-2;

$p(m_{a,b})$ is the mass function of the neutron stars. Note that we use $m_{a,b}$ instead of $m_{1,2}$. The latter are the primary and secondary stars based on their masses, while the former we do not distinguish between the primary and the secondary. We assume both m_a and m_b are following the same mass function. We use a truncated Gaussian with upper and lower cuts as the mass function. The default parameters are the mean $\bar{m} = 1.4 M_\odot$, the mass dispersion $\sigma_m = 0.5 M_\odot$, upper cut $m_{\text{cut,low}} = 1.1 M_\odot$, $m_{\text{cut,high}} = 2.5 M_\odot$; we apply also a truncated Gaussian spin model, with a smaller dispersion $\sigma_\chi = 0.05$. These simplified choices are roughly agree with observations (Valentim et al. 2011; Özel et al. 2012; Kiziltan et al. 2013; Miller & Miller 2015; Farrow et al. 2019; Zhang et al. 2019), while they can be substitute with more realistic models.

3.1.3. Neutron star/black hole mergers

For the population model of BHNS, we again assume the merger rate density to be:

$$\dot{n}(z, m_1, m_2, \chi) = \mathcal{R}(z) f(m_\bullet) p(m_n) P(\chi), \quad (8)$$

where $\mathcal{R}(z)$ is taking the same form as for BBH and DNS, with a different default setting: $\mathcal{R}_n = 45 \text{ Gpc}^{-3} \text{ yr}^{-1}$ and $\tau = 3 \text{ Gyrs}$; which is broadly consistent with the merger rate, which is implied by the number of BHNS detection in LVK O3a+b (Abbott et al. 2021a). $f(m_\bullet)$ is the mass function of the BH, which has the same function forms same as BBH. We denote the population model without/with the peak component in $f(m_\bullet)$ as BHNS-PopA/B; The default parameters for $f(m_\bullet)$ are $\mu = 3$, $\gamma = 2.5$, $c = 6$, $m_{\text{cut}} = 95 M_\odot$, $A_{\text{peak}} = 0.002$, $m_{\text{peak}} = 40 M_\odot$, $\sigma_{\text{peak}} = 1 M_\odot$. $p(m_n)$ is the mass function of the NS, which is the same as in the DNS case.

3.2. Sources for space-borne detectors

3.2.1. Supermassive Black Hole Binaries

In the last two decades, it has been established that in the center of most galaxies there is a supermassive black hole (SMBH, with mass from $10^4 M_\odot$ to $10^{10} M_\odot$). Since the mergers of galaxies are thought to be ubiquitous under the hierarchical clustering process, there are expected to be close binaries of supermassive binary black holes (SMBBH) in the merger galaxies, which emit GW during their inspiral and merger phase (e.g. Colpi 2014). Such SMBBH inspirals are the main targets of LISA (Amaro-Seoane et al. 2017), TianQin (Luo et al. 2016) and PTA (Jenet et al. 2004, 2005), since the frequency of their GW falls in the $10^{-8} - 1 \text{ Hz}$ range. We use the SMBBH merger catalogues from Klein et al. (2016) (Klein16 hereafter), which are based on Barusse (2012). There are three population models being considered, namely pop3, Q3_node1ays and Q3_de1ays. They mainly differ in the origin of their SMBH seeds, and whether the delays between SMBH mergers and galaxy mergers are included (see Klein16 for a detailed description; see also a review on supermassive BH formation and evolution by Inayoshi et al. 2020). For pop3, the SMBH seeds are from PopIII stars (light seeds), and the delay between SMBH and galaxy mergers is accounted; for Q3_node1ays and Q3_de1ays, the SMBH seeds are assumed to be from the collapse of protogalactic disks (heavy seeds). The former accounts for the delay between SMBH and galaxy mergers,

while the latter does not. For each population model, there are ten catalogues, each corresponding to a realisation of all sources in the Universe within five years. The number of total events for each population is ~ 890 for pop3, ~ 630 for Q3_node1ays and ~ 40 for Q3_de1ays. They are compatible with the reported averaged merger rates in Klein16 (pop3: 175.36 yr^{-1} , Q3_node1ays: 121.8 yr^{-1} and Q3_de1ays: 8.18 yr^{-1}). In figure 5 we plot $M_{z,\text{tot}}$ (red-shifted total mass) and z of SMBBH mergers that occur in the Universe over a timescale of five years for three population models as a direct demonstration of the population models. The distribution agrees with those shown in Fig 3 of Klein16.

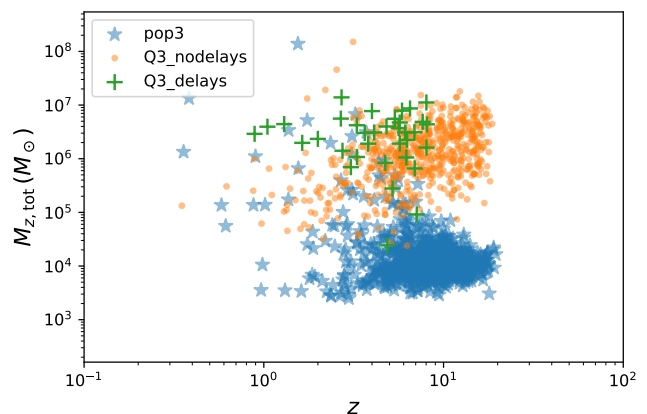


Fig. 5. $M_{z,\text{tot}}$ vs. z of SMBBH mergers that occur in the Universe over a timescale of five years for three population models from Klein16. The data corresponds to one realisation.

3.2.2. Double White Dwarfs

Another important population of LISA sources are Ultra Compact Galactic Binaries. Among those Galactic binaries, close double white dwarfs (DWDs) are the dominant, and are long expected to be promising targets for LISA and other space-borne GW detectors (e.g. Nelemans et al. 2001; Yu & Jeffery 2010; Nisanke et al. 2012; Toonen et al. 2012; Korol et al. 2017; Lamberts et al. 2019; Huang et al. 2020).

We use a synthetic catalogue of close DWD in the whole Galaxy (Nelemans et al. 2001). In figure 6 we plot the joint distribution density of the frequencies $f_s = 2/P$ (where P is the orbital period of the binaries) and the intrinsic amplitudes $A = 2(GM)^{5/3}(\pi f)^{2/3}/(c^4 d)$ of GW emitted from binaries in the catalogue. The contours mark levels which correspond to uniform iso-proportions of the density. The total number of sources in the catalogue is $\sim 2.6 \times 10^7$.

Beside the synthetic catalogue, we also include a catalogue of 81 known DWDs (Huang et al. 2020) a.k.a. verification binaries (VBs, see also Kupfer et al. 2018). Those VBs are plotted along in figure 6 with star markers. Note that the distribution of the verification binaries do not follow that of the simulated DWD in the whole Galaxy, due to very strong observational biases which favour close by sources to be detected as VBs.

3.2.3. Extreme Mass-Ratio Inspirals

In the nuclei region of galaxies, surrounding the supermassive black holes (SMBH), there are abundant stellar populations. Among them, compact objects, including stellar mass BHs, NS

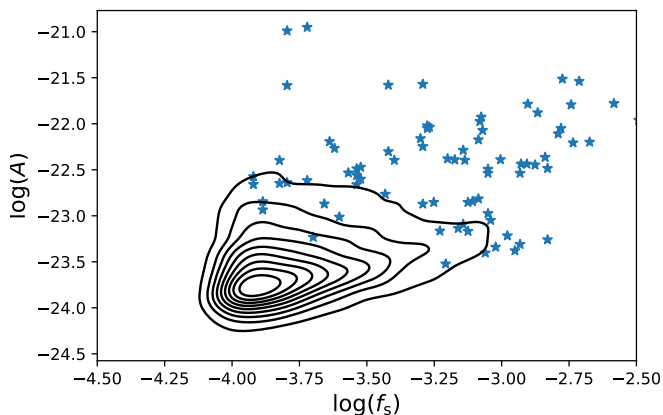


Fig. 6. The distribution density of GW properties of DWD binaries in the simulated catalogue (black contours), as function of GW frequency f_s and GW amplitude A . The blue stars are known DWDs as verification binaries.

and white dwarfs, can inspiral into the central SMBH, radiating a large amount of energy in GW. These systems are referred to as extreme mass ratio inspirals (EMRIs). EMRIs are very interesting targets for space-borne detectors such as LISA (see [Amaro-Seoane et al. 2007](#)).

In the `GW-Toolbox`, we use the simulated catalogues from [Babak et al. \(2017\)](#) (Babak17 hereafter) and use their population models M1-M11 (skipping M7, explained later). These populations differ in several ingredients: the mass function and spin distribution of SMBHs, the $M - \sigma$ relation, the ratio of plunges to EMRIs and the characteristic mass of the compact objects (see Babak17 for a detailed description of models). For each population model, there are ten realizations of the catalogues, which contain detectable EMRIs within one year with the assumption of standard LISA noise properties. The distributions of μ (mass of the stellar BH), M (mass of the massive BH) and D (luminosity distance) in the catalogues are plotted in figure 7. The histogram for each population is averaged among the ten realizations. Since we are using an SNR limited sample, instead of a complete one of the whole Universe (which is ~ 10 times larger), the `GW-Toolbox` will give an underestimated detectable number and an incomplete catalogue of detections, especially when using a lower SNR cutoff or a more sensitive LISA configuration. For now, we exclude M7 and M12 from the Toolbox, because in their population models the direct plunges are ignored, therefore the total number of EMRIs are about one order of magnitude larger than others, which will make the computation take too long.

3.3. Sources for Pulsar Timing Arrays

3.3.1. Individual Massive Black Hole

Long before (millions or tens of millions of years, depends on their chirp mass; see [Sesana & Vecchio 2010](#); [Petiteau et al. 2013](#); [Burke-Spolaor et al. 2019](#)) the GW from supermassive black hole binaries entering the band of space-borne GW detectors, it lies in the PTA frequency range. If there would be such MBH binaries sufficiently close to the Earth, PTAs could detect their signals. Since no sources are known yet, we incorporate this source class in the `GW-Toolbox` in the form of a free form in which the user can fill in the frequency and GW amplitude, and the `GW-Toolbox`

will determine if this binary, as a monochromatic GW source, can be detected by the selected PTA.

3.3.2. Stochastic background

The second class of target for PTA are Stochastic GW background (SGWB). It can originate from the incoherent overlapping of many unresolvable SMBBH ([Phinney 2001](#); [Sesana et al. 2008](#); [McWilliams et al. 2014](#)), the relic of primordial GW ([Grishchuk 1976, 1977](#); [Linde 1982](#); [Starobinsky 1980](#)), or the collision of cosmic-strings ([Damour & Vilenkin 2001, 2005](#); [Siemens et al. 2006, 2007](#); [Ölmez et al. 2010](#)). Each of these gives rise to a power-law GW signal

$$h_c^2(f) = C f^\gamma, \quad (9)$$

where the index γ corresponds to the origin of SGWB. For incoherent overlapping of SMBBH, $\gamma = -2/3$; for relic GW, $\gamma = -1$ and for cosmic-strings, $\gamma = -7/6$. We also enable users to customize γ .

4. Implementation 2: Gravitational Wave detectors

4.1. Ground-based interferometers

4.1.1. Noise model of interferometers

For ground-based interferometers, the `GW-Toolbox` integrates the design performance of advanced LIGO (aLIGO), Advanced Virgo (AdV), KAGRA, CE and ET instruments. The noise models for the above-mentioned interferometers are taken from the following resources:

- aLIGO: <https://dcc.ligo.org/LIGO-T1800044/public>, see also [The LIGO Scientific Collaboration et al. \(2015\)](#);
- adV and KAGRA: <https://dcc.ligo.org/LIGO-T1500293/public>;
- CE: <https://dcc.ligo.org/LIGO-P1600143/public>;
- ET: <http://www.et-gw.eu/index.php/etsensitivities>, see also [Hild et al. \(2008, 2010, 2011\)](#);

In the upper panel of figure 8, we plot the noise curves that are used for the default detectors. aLIGO-O3 corresponds to the noise performance in O3 period, while aLIGO-design is the designed sensitivity of the aLIGO; CE1 and CE2 correspond to the expected first and second stages of CE respectively; for ET we use the ET-D-sum curve.

In addition, the `GW-Toolbox` employs the package FINESSE to calculate S_n of a LIGO-like or a ET-like interferometer with customised settings ([Brown et al. 2020](#)). Users can define the following parameters of the detector:

- Arm Length
- Laser power
- Arm mirror mass
- Arm mirror transmission coefficient
- Signal recycling mirror transmission coefficient
- Power recycling mirror transmission coefficient
- Signal recycling phase factor
- Power recycling cavity length

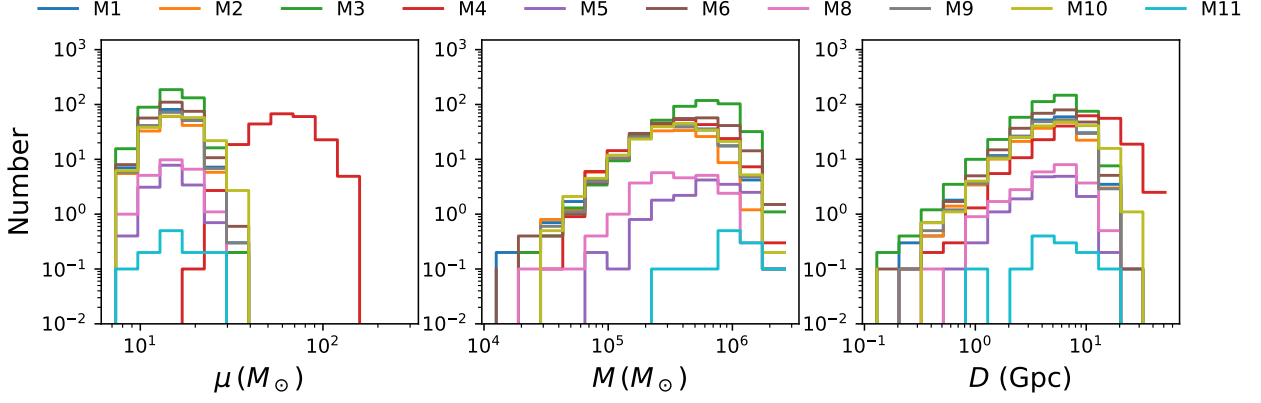


Fig. 7. The averaged histograms of μ , M and D of EMRIs happen in one year, assuming different population models from Babak17

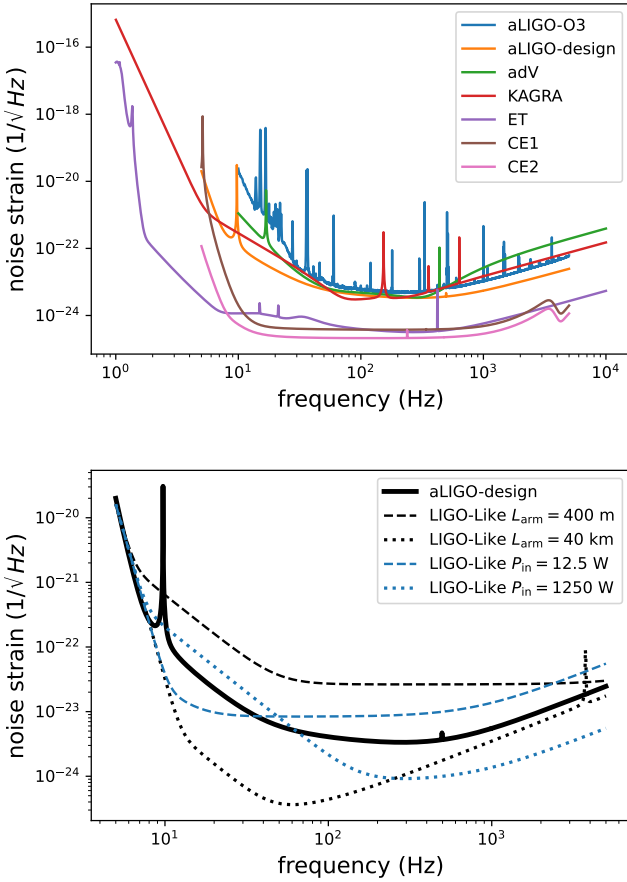


Fig. 8. Upper Panel: Noise Curves of the default detectors: aLIGO-O3 corresponds to the noise performance in O3 period, while aLIGO-design is the designed sensitivity of the aLIGO; CE1 and CE2 correspond to the expected first and second stages of CE respectively; ET-D-sum curve is applied for ET. **Lower Panel:** aLIGO in design vs. Customised settings (arm length=4 km, laser power=125 W)

– Signal recycling cavity length

The most important parameters that affect the sensitivity are the arm length and laser power. In the lower panel of figure 8, we show the effects of varying the arm length and the laser power starting from the design aLIGO sensitivity. One of the other influential parameters is the mass of the arm mirror. Heavier arm

mirrors will decrease the noise in the low frequency ends slope and leave the high frequency end unaffected.

4.1.2. SNR of GW from compact binary merger

The core of the method with which the GW-Toolbox determines detectability of sources is to compare the SNR threshold ρ_* with that of a source, which can be calculated with (Maggiore 2008):

$$\rho^2 = 4 \int_{f_{\text{low}}}^{f_{\text{high}}} \frac{|h^2(f)|}{S_n(f)} df, \quad (10)$$

where $h(f)$ is the frequency domain response of the interferometer to the GW signal, and S_n is the noises power density. For a binary system, the detector response can be expressed as³:

$$h(f) = C \sqrt{\left(\frac{1 + \cos^2 \iota}{2}\right)^2 F_+^2 + \cos^2 \iota F_\times^2} A(f) e^{-i(\Psi(f) + \phi_p)}. \quad (11)$$

In the above equation, the constant

$$C = \frac{1}{2} \sqrt{\frac{5}{6}} \frac{(GM)^{5/6}}{c^{3/2} \pi^{2/3} D_L}, \quad (12)$$

where M is the red-shifted chirp mass of the binary, D_L is the luminosity distance, ι is the inclination angle between the orbital angular momentum and the line of sight; $A(f)$ is the frequency dependence of the GW amplitude. As a proof of principle of the GW-Toolbox, we apply the waveform approximant, which has hybrid degrees of simplification. For the amplitude $A(f)$, we use a broken power-law:

$$A(f) = \begin{cases} f^{-7/6}, & f \leq f_{\text{trans}}, \\ f^{-2/3}, & w_m f_{\text{trans}} < f \leq f_{\text{cut}}, \\ 0, & f \geq f_{\text{cut}}, \end{cases} \quad (13)$$

where w_m is the scaling factor that to make $A(f)$ continuous. The above formula represents the inspiral, merger and ring-down

³ in general, the detector response to the (ℓ, m) multipole mode is

$$h^{\ell m} = F_+ h_+^{\ell m} + F_\times h_\times^{\ell m}.$$

When we limit the waveform to the dominant (quadrupole) mode, the response takes the form in equation 10, with the terms $(1 + \cos^2 \iota)/2$, $\cos \iota$ from the h_+^{22} and h_\times^{22} respectively. For expressions of higher order mode $h_{+,\times}^{\ell m}$, see Mehta et al. (2017); Mills & Fairhurst (2021). We discuss the influence of including the higher order modes in Section 6.

phases of a circular, non-spinning point mass binary. It corresponds to the $A(f)$ in the approximant IMRPhenomD (Ajith et al. 2011), when the effective spin $\chi = 0$. The transition frequency f_{trans} and the cut-off frequency f_{cut} corresponds to f_1 and f_2 of Ajith et al. (2011). $A(f)$ and m_1, m_2 and D via C essentially determine the SNR of sources, because the effective spin has a much weaker effect on the SNR. Therefore the dependence on χ can be separated from that on m_1, m_2 and D . It makes the catalogue sampling process easier and more effective (the Markov Chain mixes faster with less dimension, see below).

$\Psi(f)$ is the phase of the waveform. It is essential for evaluating the uncertainties on the intrinsic parameters. Therefore we use $\Psi(f)$ from the frequency domain waveform IMRPhenomD (Ajith et al. 2011) and restore its dependency on χ . It corresponds to a hybrid waveform of a circular binary with parallel spin, that matches post Newtonian and numerical relativity waveforms.

$F_{+,x}$ are the antenna patterns of the interferometer, which are function of position angles of the source (θ, φ) and the polarization angle of the GW ψ . For LIGO/Virgo/KAGRA-like interferometers, which have two perpendicular arms, the antenna patterns are:

$$\begin{aligned} F_{+,90^\circ} &= \frac{1}{2}(1 + \cos^2 \theta) \cos 2\varphi \cos 2\psi + \cos \theta \sin 2\varphi \sin 2\psi \\ F_{\times,90^\circ} &= \frac{1}{2}(1 + \cos^2 \theta) \cos 2\varphi \sin 2\psi + \cos \theta \sin 2\varphi \cos 2\psi, \end{aligned} \quad (14)$$

and for ET-like interferometers with 60° angles between the arms (Regimbau et al. 2012):,

$$\begin{aligned} F_{+,60^\circ} &= -\frac{\sqrt{3}}{2} F_{+,90^\circ} \\ F_{\times,60^\circ} &= \frac{\sqrt{3}}{2} F_{\times,90^\circ}. \end{aligned} \quad (15)$$

ET will have three nested interferometers, 60° rotated with respect to each other. The antenna pattern for each interferometers are $F_{i+,x}(\theta, \varphi, \psi) = F_{0+,x}(\theta, \varphi + 2/3i\pi, \psi)$, where $i = 0, 1, 2$ is the index of the interferometers, and $F_{0+,x}$ are those in equation (15). The joint response can be calculated with equation (11), where the antenna pattern squared should be substituted with:

$$F_{+,x}^2 = \sum_{i=0}^2 F_{i+,x}^2. \quad (16)$$

In our treatment, the modulation on the antenna patterns due to the Earth rotation is neglected, for the duration of the GW signal is typically much less than the period of Earth rotation. The situation would change for 3G detectors, which has much broader frequency window and the ability to better resolve the waveform.

4.1.3. Determining the sample of detected sources

Given the differential cosmic merger rate density for compact binary mergers \dot{n} , the theoretical number distribution for each source class in the catalogue is:

$$N_D(\Theta, \theta, \varphi, \psi, \iota) = \frac{\Delta T}{1+z} \frac{dV_c}{4\pi dz} \dot{n}(\Theta, \theta, \varphi, \iota, \psi) \mathcal{H}(\rho^2 - \rho_\star^2). \quad (17)$$

where ΔT is the time span of observation, dV_c/dz is the differential cosmic comoving volume (volume per redshift), \mathcal{H} is the Heaviside step function and ρ_\star is the SNR threshold, Θ denotes

the intrinsic parameters and the luminosity distance of the source. Marginalising over the directional parameters and assuming that \dot{n} is isotropic yields

$$N_D(\Theta) = \frac{T}{1+z} \frac{dV_c}{dz} \dot{n}(\Theta) \mathcal{D}(\Theta), \quad (18)$$

where

$$\mathcal{D}(\Theta) = \iint d\Omega d\Omega' \mathcal{H}(\rho^2 - \rho_\star^2)/(4\pi)^2, \quad (19)$$

is the detectability of the source, which is determined by the detector properties and the waveform of the source. Since we use the same waveform for BBH, DNS and BH-NS, the difference among these three populations are only in the cosmic merger rate \dot{n} discussed above in Sections 3.1.1-3.1.3.

The total number of expected events catalogue is:

$$N_{\text{tot}} = \int d\Theta N_D(\Theta), \quad (20)$$

and the number of detections thus is Poisson realisation of the expectation value $N_D(\Theta)$. The synthetic catalogue is then obtained by a Markov Chain-Monte Carlo sampling from $N_D(\Theta)$. We apply the elliptical slice sampling algorithm (Murray et al. 2010), which converges faster to the target distribution comparing with the traditional Metropolis-Hasting algorithm (Neal et al. 1999) and requires less tuning on the initial parameters.

We also give the estimated uncertainties on the parameters using the Fisher Information Matrix (FIM): the covariance matrix is related to the Fisher matrix with:

$$\langle \delta\Theta_i \delta\Theta_j \rangle = \mathcal{F}_{ij}^{-1}, \quad (21)$$

where the Fisher matrix is defined as:

$$\mathcal{F}_{ij} = (\partial h / \partial \Theta_i | \partial h / \partial \Theta_j). \quad (22)$$

The partial derivatives in the above equation are calculated numerically:

$$\frac{\partial h}{\partial \Theta_i} = \frac{h(\Theta_i + \Delta\Theta_i) - h(\Theta_i - \Delta\Theta_i)}{2\Delta\Theta_i}. \quad (23)$$

In the GW-Toolbox, we use $\Delta\Theta_i = 10^{-8}\Theta_i$, as it is small enough to give stable results. We only calculate the FIM for intrinsic parameters ($m_{1,z}$, $m_{2,z}$ and χ) and an overall scaling factor that represents the effect of all extrinsic parameters. As a result, we cannot give an estimate of the uncertainties of extrinsic parameters, i.e., the distance, sky locations, inclination and polarization angle, for these parameters contribute to the overall scaling factor in a highly correlated way. In reality, the sky locations are determined largely by triangulation with a network of detectors, and the precision of other extrinsic parameters are also depended on triangulation. In the current version of the GW-Toolbox we do not include a detector network. The calculation of FIM is thus simplified. However, in order to obtain an estimation on the uncertainties on the source frame masses, one still needs to propagate the uncertainties on the redshift. The uncertainties on the redshift itself is also an interesting quantity that users want to obtain from the synthetic catalogue of GW-Toolbox. We give evaluation on δz from empirical relations. For 2G detectors, we use $\delta z = 0.5z$ roughly represents the trend of $\delta z - z$ in GWTC-3; for 3G detectors, we use $\delta z = 0.017z + 0.012$, which is a fit from the simulation results of Vitale & Evans (2017). δz is propagated

to the uncertainties on the source frame masses with the following equation:

$$\delta m_i = m_i \sqrt{\left(\frac{\delta m_{i,z}}{m_{i,z}}\right)^2 + \left(\frac{\delta z}{1+z}\right)^2}. \quad (24)$$

It is worth mentioning that although FIM is a quick, simple and widely applied method of uncertainties, it something gives over-estimated uncertainties comparing with those from full Bayesian inference (e.g. [Veitch et al. 2015](#)), especially for events with low SNR (e.g. [Vallisneri 2008](#); [Rodriguez et al. 2013](#)).

The returned catalogue is composed by the mean values of the parameters and their estimated uncertainties. A more realistic simulation of the observed catalogue can be obtained by shifting the mean values according to the corresponding uncertainties, which is straightforward and easy. Since the uncertainties given here are conservative, the `GW-Toolbox` return the un-shifted catalogue, and let the user to decide whether or how to further shift the catalogue.

4.2. Space-borne interferometers

The Space-borne interferometers module of the `Toolbox` enables users to simulate observations with LISA-like space-borne GW observatories (see [Barke et al. 2015](#)). We work with the codes of the LISA Data Challenge (LDC, <https://lisa-ldc.lal.in2p3.fr>, a successor program of the earlier Mock LISA Data Challenge ([Babak et al. 2010](#))), and make it possible for users to customize the arm length, the laser power and the telescope diameter of LISA. In the ground-based interferometers section the theoretical probability distribution of parameters of the detectable sources are first calculated, afterwards samples are drawn from such distribution as synthetic catalogues of observations. The procedure for LISA-like detectors is different: we go through pre-generated synthetic catalogues of different source populations in the whole Universe/Galaxy and calculate the SNR of each source to be detected by LISA. The SNR is still calculated with:

$$\rho^2 = 4 \int \frac{|h^2(f)|}{S_n(f)} df, \quad (25)$$

where $h(f)$ is the LISA response to a waveform of a source, and $S_n(f)$ is the noise power spectrum density (PSD). The time-delay interference (TDI) channels are combinations of data streams such that the noises arising from the fluctuation of the laser frequency can be exactly cancelled while the signal in GW can be preserved ([Tinto & Armstrong 1999](#); [Armstrong et al. 1999](#); [Estabrook et al. 2000](#)). In the `GW-Toolbox`, we consider the LISA responses and the noise spectral density in the first generation TDI-X channel ([Armstrong et al. 1999](#)). The noise spectrum will be introduced in the next section. Three classes of sources are included in the `GW-Toolbox` for LISA, namely: mergers of SMBBH, resolved DWDs in the Galaxy and EMRIs. Waveforms and the corresponding LISA responses will be introduced in the following subsections. Examples of synthetic observations are given and compared with the literature in Section 5. Uncertainties of the parameters are again estimated with the FIM method.

4.2.1. Noise TDI

The PSD of the noise TDI-X response is formulated as ([Armstrong et al. 1999](#)):

$$S_X(f) = [4 \sin^2(2x) + 32 \sin^2 x] S_y^{\text{accel}} + 16 \sin^2 x S_y^{\text{optical}}, \quad (26)$$

where $x = 2\pi fL/c$, and L is the arm length of LISA and c is the speed of light, S_y^{accel} and S_y^{optical} are the fractional frequency fluctuations due to the acceleration noise of the spacecrafts and the optical meteorology system noise respectively. For the acceleration noise, we use ([Amaro-Seoane et al. 2017](#)):

$$S_a^{\text{accel}} = 9 \times 10^{-30} \frac{[\text{m s}^{-2}]^2}{[\text{Hz}]} \left(1 + \left(\frac{[0.4\text{mHz}]}{f}\right)^2\right) \left(1 + \left(\frac{f}{[8\text{mHz}]}\right)^4\right). \quad (27)$$

Note that the above noise is in the form of acceleration. To convert it into a fractional frequency fluctuation, one needs to divide it by a factor $4\pi^2 f^2 c^2$ ([Armstrong et al. 1999](#)), resulting in

$$S_y^{\text{accel}} = \frac{3.9 \times 10^{-44}}{[\text{Hz}]} \left(1 + \left(\frac{[0.4\text{mHz}]}{f}\right)^2\right) \left(\left(\frac{[8\text{mHz}]}{f}\right)^2 + \left(\frac{f}{[8\text{mHz}]}\right)^2\right). \quad (28)$$

$$= \frac{3.9 \times 10^{-44}}{[\text{Hz}]} \left(1 + \left(\frac{[0.4\text{mHz}]}{f}\right)^2\right) \left(\left(\frac{[8\text{mHz}]}{f}\right)^2 + \left(\frac{f}{[8\text{mHz}]}\right)^2\right). \quad (29)$$

The noise of the optical metrology system can be split

$$S_y^{\text{optical}} = S^{\text{ops}} + S^{\text{opo}}, \quad (30)$$

where S^{ops} is the laser shot noise, which scales with the arm length L , the laser power P and the diameter of the telescope D as ([Amaro-Seoane et al. 2017](#)):

$$S^{\text{ops}} = 5.3 \times 10^{-38} \times \left(\frac{f}{[\text{Hz}]}\right)^2 \frac{[2\text{W}]}{P} \left(\frac{L}{2.5[\text{Gm}]}\right)^2 \left(\frac{[0.3\text{m}]}{D}\right)^2 \text{Hz}^{-1}; \quad (31)$$

and

$$S^{\text{opo}} = 2.81 \times 10^{-38} (f/[\text{Hz}])^2 \text{Hz}^{-1} \quad (32)$$

denotes the contribution from other noise in the optical meteorology system.

We also include the TDI-X noise PSD originating from the foreground GW emission from Galactic DWDs (GWD). In practice this confusion noise will be modulated with the orbital phase of the spacecraft. For simplicity, we adopt an analytic approximation for the averaged equal-arm Michelson PSD of GWD as ([Robson et al. 2019](#)):

$$S_{\text{GWD}}(f, T_{\text{obs}}) = A f^{-7/3} e^{-f^\alpha + \beta f \sin(\kappa f)} (1 + \tanh(\gamma(f_k - f))), \quad (33)$$

Note that the noise depends on the observation duration, because for longer observations, more and more individual DWDs can be resolved and removed from the confusion noise foreground. This time dependent is represented by using different parameters with different T_{obs} as shown in table 1. The amplitude A is fixed at 9×10^{-45} for $T_{\text{obs}} \leq 4$ years, and is set to zero for larger T_{obs} since the foreground then disappears.

The equal-arm Michelson response (fractional displacement) PSD term S_{GWD} can be converted to the fractional frequency by timing a factor x^2 and then added to S^{ops} calculated with equation (26). The upper panel of figure 9 shows the square root of the noise PSD with various LISA parameters. Note that our S_X should not be confused with the PSD in the Michelson response. The latter is more commonly applied and sometimes referred as the sensitivity curve. The `GW-Toolbox` also provide the latter with the following analytic model ([Robson et al. 2019](#)):

$$S_n = \frac{10}{3L^2} \left(S_{\text{dis}}^{\text{op}} + 2(1 + \cos^2(x)) \frac{S_a^{\text{acc}}}{(2\pi f)^4} \right) \left(1 + \frac{3}{5} x^2\right) + S_{\text{GWD}},$$

	≤6 mo	≤1 yr	≤2 yr	≤4 yr
α	0.133	0.171	0.165	0.138
β	243	292	299	-221
κ	482	1020	611	521
γ	917	1680	1340	1680
f_k	0.00258	0.00215	0.00173	0.00113

Table 1. The parameters of the confusion noise of the unresolved GWD background.

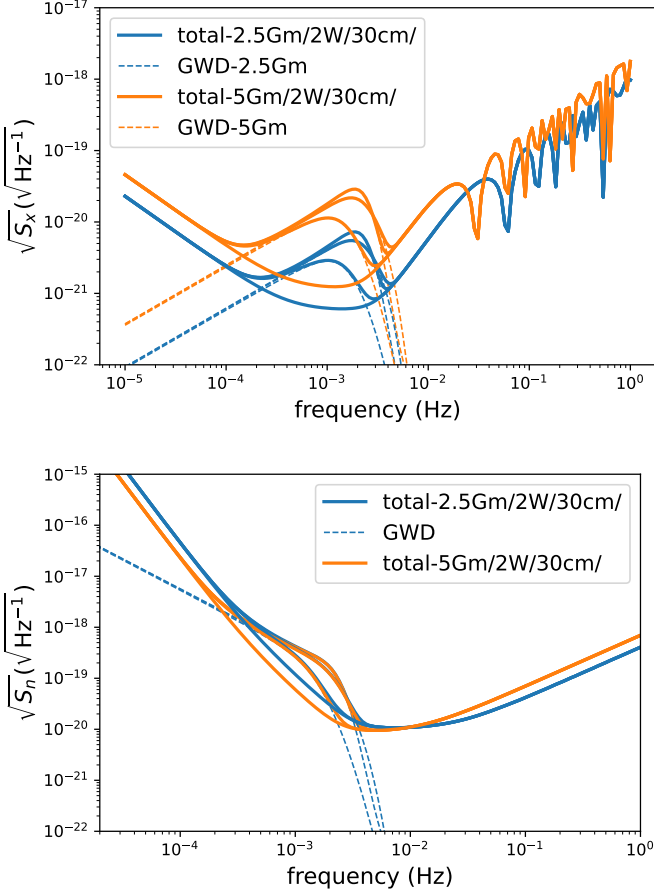


Fig. 9. Upper Panel: Square root of the PSD noise TDI-X corresponding to different LISA configurations. The solid curves are the total PSD, while the dashed curves are the contribution from the confusion GWDs. The bundle of curves in the same colour correspond to $T_{\text{obs}} = 1, 2, 4, 5$ years from top to bottom; **Lower Panel:** Sensitivity curves corresponding to different arm length and T_{obs} . The solid curves are the total curve, while the dashed curves are the contribution from the confusion GWDs. The bundle of curves in the same colour correspond to $T_{\text{obs}} = 1, 2, 4, 5$ years from top to bottom.

where $S_{\text{dis}}^{\text{op}}$ is the noise in the optical system in term of the displacement, which can be converted into the previous Doppler S_y^{optical} by multiplication by a factor $2\pi f/c$. We plot the sensitivity curves corresponding to different arm length and T_{obs} in figure 9. In the appendix, we give a summary plot of the conversion among different detector responses.

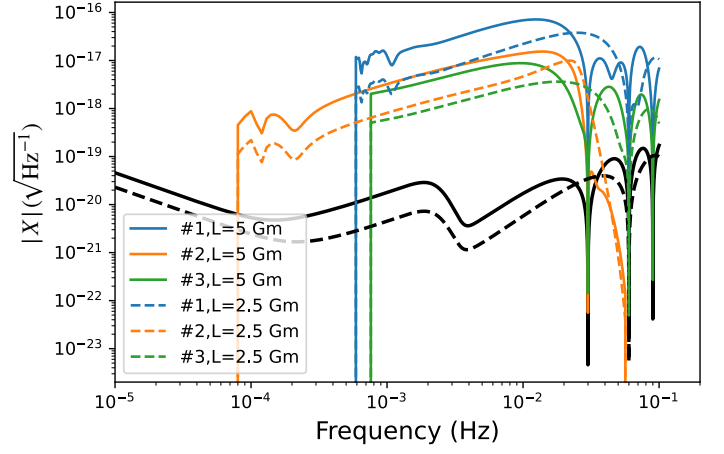


Fig. 10. Modulus of frequency domain TDI-X responses to GW from different SMBBHs (whose parameters are listed in Table 2). The solid curves correspond to LISA with 5 Gm laser arms, and dashed curves correspond to a 2.5 Gm arms configuration.

4.2.2. TDI response to the SMBBH waveform

The TDI-X response of LISA due to a GW from a SMBBH merger is calculated using the LDC code (Babak et al. 2010), where the IMRPhenomD waveform is adopted (Ajith et al. 2011). Figure 10 shows the modulus of the TDI-X responses in the frequency domain, for three different sources. The parameters of the example sources are listed in Table 2. The low-frequency limit corresponds to the time to coalescence at the beginning of the observation, and the dips at the high frequency end are due to the term $\sin(x)$ when converting to TDI. The sample cadence is fixed to 5 s, which corresponds to a high frequency cut-off at 0.1 Hz. For systems with heavy BHs, like #2 in the example (masses $> 10^5 M_{\odot}$), the frequency at coalescence is lower than the cut-off frequency, therefore the current cadence will not lose any power from the signal; On the other hand, for systems with light BHs, like #1 in the example (masses $< 50,000 M_{\odot}$), the high frequency part (> 0.1 Hz) of the waveform will be lost. However, the decrease of SNR is less than 1% comparing to that using a cadence of 1 s. Therefore it is acceptable to fix the cadence to 5 s for all sources, in order to perform the simulation fast.

4.2.3. TDI Waveform of DWD

We first derive the frequency domain TDI-X waveform in a monochromatic plane wave approximation. The equal-arm Michelson response of a plane GW in the long-wavelength region can be approximated as a sine wave with a orbit averaged amplitude $\langle \mathcal{A} \rangle$ and frequency f_s . The relation between $\langle \mathcal{A} \rangle$ and the intrinsic amplitude A of the source binary can be found in equations (A12,A13) of Korol et al. (2017).

The Fourier transform of such a signal with the duration T_{obs} is:

$$(34) \quad \tilde{h}_{\text{Mich}}(f) = \frac{1}{2} \langle \mathcal{A} \rangle T_{\text{obs}} \text{sinc}((f - f_s)T_{\text{obs}}). \quad (35)$$

Note that here we use the convention that $\text{sinc}(x) = \sin(\pi x)/(\pi x)$, such that the integration of $|\tilde{h}(f)|^2$ equals $T_{\text{obs}} A^2$.

To convert the equal-arm Michelson into TDI-X, we multiply by a factor $4x \sin x$, where $x = f(2\pi L/c)$.

$$X(f) = 2x \sin x \langle \mathcal{A} \rangle T_{\text{obs}} \text{sinc}[(f - f_s)T_{\text{obs}}] \quad (36)$$

#	β (rad)	λ (rad)	θ_{χ_1} (rad)	θ_{χ_2} (rad)	φ_{χ_1} (rad)	φ_{χ_2} (rad)	χ_1	χ_2	$m_1 (M_\odot)$	$m_2 (M_\odot)$	θ_L (rad)	φ_L (rad)	z	t_c (yr)
1	-1.3	0.44	0.8	2.6	4.5	5.98	0.8	0.2	37695	4582	2.18	1.3	0.069	0.76
2	-0.44	4.7	0.08	0.037	4.26	5.48	0.04	0.2	420555	298237	1.14	3.26	5.1	0.0038
3	-0.01	2.7	0.12	0.12	0.72	6.08	0.6	0.13	76476	28854	1.673	1.47	2.8	0.5

Table 2. Parameters of example sources corresponding the figure 10. The meaning of the parameters are: β -Ecliptic Latitude; λ -Ecliptic Longitude; θ_{χ_1/χ_2} -Polar angle of spin 1/2; $\chi_{1,2}$ -Spin 1/2; $m_{1,2}$ -(Intrinsic) masses of primary/secondary BH; θ_L -Initial polar Angle of the orbital angular momentum; φ_L Initial azimuthal Angle of the orbital angular momentum; z red-shift; t_c time to coalescence at the beginning of observation;

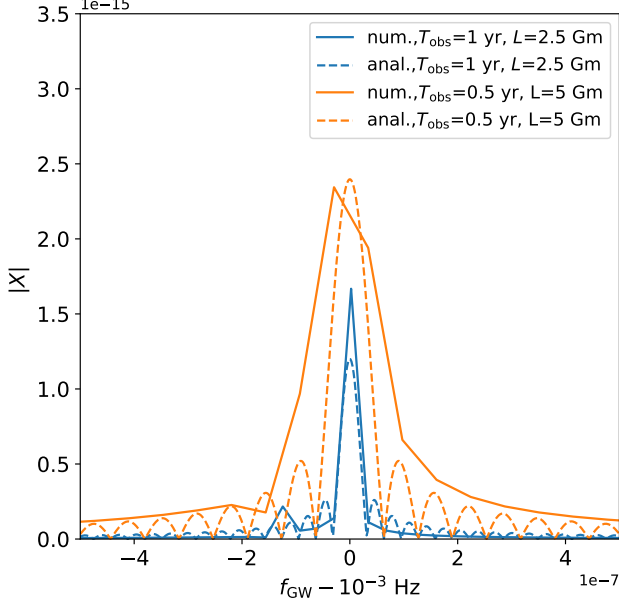


Fig. 11. Frequency domain LISA responses to GW from a DWD: The blue and oranges lines correspond to two different LISA configurations; solid and dashed lines correspond to responses calculated with numerical and analytical methods respectively.

In figure 11 we show the waveforms of a DWD with $A = 10^{-20}$, $f_s = 10^{-3}$ Hz, calculated analytically from equation (36) and compare them with those calculated numerically with the LDC code (which is based on Cornish & Littenberg 2007). Although simplified, the overall agreement between the two is good.

From equations (25,36), we obtain an approximated squared SNR expression:

$$\rho_{\text{approx.}}^2 = \frac{16x^2 \sin^2 x \langle \mathcal{A}^2 \rangle T_{\text{obs}}}{S_X(f_s)}. \quad (37)$$

When we replace the TDI- X noise PSD with the Michelson noise PSD, and drop the $16x^2 \sin^2 x$ term, the above equation becomes equation (10) of Korol et al. (2017).

4.2.4. TDI Waveform for EMRIs

The analytic kludge (AK) waveforms (Barack & Cutler 2004) for EMRIs are applied and the corresponding TDI- X responses are calculated with the code package EMRI_Kludge_Suite⁴ (Chua & Gair 2015; Chua et al. 2017). As examples, in figure 12 we plot the frequency domain TDI- X responses to the AK waveforms, which correspond to three EMRIs systems and two L designs of

⁴ https://github.com/alvincjk/EMRI_Kludge_Suite

LISA. The first system (blue curves) has a supermassive BH with mass $M = 10^6 M_\odot$ and stellar mass BH with mass $m = 20 M_\odot$. Here the masses are all measured in the observer's frame, i.e., red-shifted. The frequency domain response corresponds to a time-domain waveform simulated from the semi-latus rectum $p = 8GM/c^2$ to the final plunge. The time resolution is $dt = 25$ s, which is set to ensure that the highest frequency cut-off set by $1/(2dt)$ is larger than the Kepler frequency around the innermost stable circular orbit (ISCO) of the supermassive BH. The lower frequency cut corresponds to initial orbital inspiral, and the higher frequency cut corresponds to the orbital frequency at the plunge, which approximates to the Kepler frequency at ISCO; The second system (orange curves) has a supermassive BH with mass $M = 10^5 M_\odot$ and stellar mass BH with mass $m = 20 M_\odot$. The initial semi-latus rectum is also $p = 8GM/c^2$. Since the Kepler frequency at ISCO is inversely proportional to the mass of the supermassive BH, we use $dt = 2.5$ s. The third system (green curves) is identical with the second one. The difference is the initial semi-latus rectum of the third one is $p = 20GM/c^2$. To track the evolution from this larger initial semi-latus rectum to the final plunge, the simulation includes ~ 10 times longer time steps. As a result, more low-frequency components are included in the third waveforms than the second. Other physical parameters are identical for the three system and are (values used in parenthesis) (Barack & Cutler 2004):

- s : dimension-less spin of the massive BH ($s = 0.5$);
- e : the initial eccentricity ($e = 0$);
- ι : the initial inclination ($\iota = 0.524$ rad);
- γ : the pericenter angle in AK Waveform ($\gamma = 0$);
- ψ : the initial phase ($\psi = 0.785$ rad);
- θ_S : the sky position polar angle of source in an ecliptic-based coordinate system, equals to $\pi/2$ minus the ecliptic latitude ($\theta_S = 0.785$ rad);
- ϕ_S : the sky position azimuth angle of source in an ecliptic-based coordinate system, equals to the ecliptic longitude ($\phi_S = 0.785$ rad);
- θ_K : the polar angle of the massive BH spin ($\theta_K = 1.05$ rad);
- ϕ_K : the azimuth angle of the massive BH spin ($\phi_K = 1.05$ rad);
- α : the azimuthal direction of the orbital angular momentum ($\alpha = 0$);
- D : luminosity distance ($D = 1$ Gpc).

As mentioned above, if the frequency domain waveform were to be simulated in real time for every candidate event, it is difficult to reconcile both the speed of simulation and to include the full GW signal from the beginning of the observation to the plunge. As a solution, we generate the frequency domain TDI waveform corresponding to each candidate event in the catalogue in advance, and store their modulus in files. The pre-generated TDI waveform corresponds to signal from the beginning of the observation to the final plunge. The initial semi-latus is calculated with a Newtonian formula equation 4.136 of Maggiore (2008) according to its masses, eccentricity and time to plunge at the

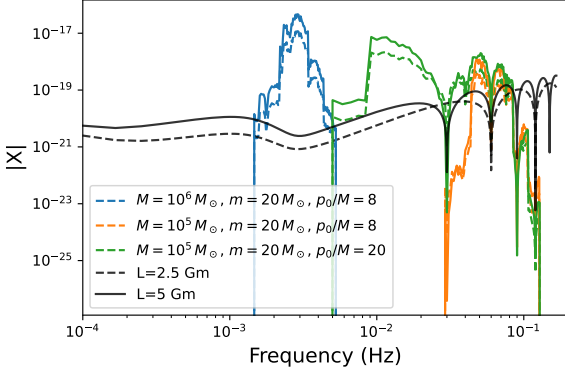


Fig. 12. Frequency domain TDI-X responses to EMRI AK waveform, which correspond to three EMRIs systems and two L designs of LISA

beginning of observation. The pre-calculated TDI corresponds to a LISA arm length 2.5 Gm. The conversion to a different LISA arm length can be done by rescaling with $x_{1,i} \sin x_{1,i} / (x_{0,i} \sin x_{0,i})$, where:

$$x_{0,i} = 2\pi f_i L_{\text{default}} / c, \quad (38)$$

and

$$x_{1,i} = 2\pi f_i L_{\text{new}} / c. \quad (39)$$

4.3. Pulsar Timing Arrays

Pulsars are rotating neutron stars. Some of the known pulsars which are very stable, i.e., their spin period only changes a tiny fraction in a very long epoch. Therefore, the arrival time of each pulse from such a pulsar can be modeled with high precision. The passing of a series of GW will cause additional changes to the expected time of arrival of the pulses (TOAs), and thus provide a way to detect GW, at frequencies between 10^{-8} and 10^{-5} Hz, where the lower frequency limit corresponds to the observation span of years, and the high frequency limit corresponds to the average cadence of a couple of days (see Sazhin 1978; Detweiler 1979; Hellings & Downs 1983; Jenet et al. 2005). A pulsar timing array is a group of pulsars, which are stable and have been monitored with radio telescopes for a long time. The existing PTA consortia are EPTA (Kramer & Champion 2013), PPTA (Hobbs 2013), NANOGrav (McLaughlin 2013) and IPTA (Hobbs et al. 2010). The standard procedure of pulsar timing is to first fit a timing model to the TOAs of individual pulsars, that includes inaccuracies in the pulsars' astrometric parameters, a model for spin evolution, refractive effects of interstellar medium and solar wind, the orbital and spin motion of the Earth, delays due to general relativity *etc.* (see Hobbs et al. 2006). The difference between the timing model and the observed TOAs, the timing residuals, are used to extract information about possible GW signals with frequentist (Jenet et al. 2005; Babak & Sesana 2012; Ellis et al. 2012) or Bayesian methods (van Haasteren et al. 2009; Ellis 2013). Here we want to use a simplified way to represent the properties of PTAs, without the need to make use of the full time series of the timing residuals, and obtain results which agree to an order of magnitude with the published results. We base our method on measuring the excess power from GW over analytic timing noise power spectra. Such a practice was also used by some early work (Jenet et al. 2004; Yardley et al. 2010; Yi et al. 2014).

4.3.1. Representing the timing noises

Suppose that we have already removed every known effect that contributed to differences in the TOAs, the timing residuals that remain are purely intrinsic to the pulsars due to their spin irregularity. Previous studies found that such timing noise can be decomposed into a red noise component and a white noise component (Hobbs et al. 2010). The red noise component can be represented with a power-law spectrum, with increasing power towards the lower frequencies, while the white noise component has a frequency independent power level. In the GW-Toolbox, we use the following equation to represent the noise spectrum density of the timing residuals of an individual pulsar:

$$S_{\text{total}}(f) = \sigma_w^2 / (f_{\text{high}} - f_{\text{low}}) + S_{\text{n,red}}(f), \quad (40)$$

where σ_w is the level of the white noise, $f_{\text{high}} = N/(2T)$ is the high frequency cut-off defined by the observation cadence and $f_{\text{low}} = 1/T$ is the low frequency cut-off defined by the inverse of the duration, $S_{\text{n,red}}(f)$ is the red noise component, which has a power-law form:

$$S_{\text{n,red}}(f) = \frac{A_{\text{red}}^2}{12\pi^2} \left(\frac{f}{\text{yr}^{-1}} \right)^{-\alpha}. \quad (41)$$

Therefore, we define the noise spectrum of a pulsar with five parameters, namely: N the number of observations, T the duration of observation, A_{red} the normalization of the red noise, α the power index of the red noise, and σ_w the level of the white noise. The last three are intrinsic properties of the pulsar. These parameters for the pulsars in the above mentioned PTAs are fitted and published (Desvignes et al. 2016; Porayko et al. 2019; Alam et al. 2020). The GW-Toolbox includes 42 pulsars in EPTA, 26 pulsars in PPTA, 47 pulsars in NANOGrav and 87 pulsars in IPTA. Besides the pulsars in the current PTAs, the GW-Toolbox also includes simulated future observations, with customised observation cadence and duration, and an increasing number of newly discovered pulsars during the observation period. The parameters (sky coordinates RA, DEC and noise parameters A_{red} , α , σ_w) of the simulated pulsars are assigned in the following way: randomly select two pulsars from the current PTA with replacement, and draw a uniformly random number between the parameters of the selected pair of pulsars, and assign the random variable as the corresponding parameter of the new pulsar. In this method, the noise properties and sky distribution of the new pulsars reflect those of the known pulsars.

In figure 14, we plot the noise spectra density of pulsars in the PTAs used by the GW-Toolbox. Blue curves correspond to known pulsars in existing PTAs, and orange curves are simulated new pulsars. In figure 13, we plot the sky coordinates of pulsars in the PTA. The blue dots indicate the pulsars from IPTA, and orange dots indicate simulated new pulsars. The size of the markers is proportional to the number of TOAs of the corresponding pulsar.

4.4. PTA detections

The GW from an individual supermassive BH can be approximated with a monochromatic wave. The timing residuals induced in the i -th pulsar is (Yi et al. 2014):

$$\mathcal{A}_i = \frac{h_s}{\omega} (1 + \cos \theta) \sqrt{\cos^2 2\psi \left(\frac{1 + \cos^2 \iota}{2} \right)^2 + \sin^2 2\psi \cos^2 \iota} \quad (42)$$

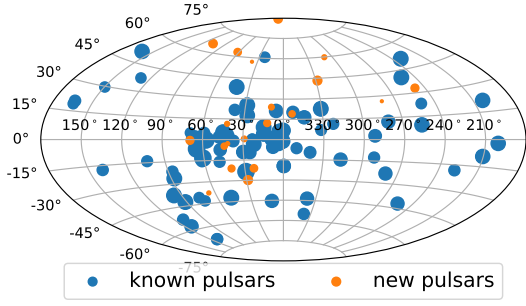


Fig. 13. Galactic distribution of the PTAs. The blue dots indicate the pulsars from current IPTA, and orange dots indicate simulated new pulsars. The size of the markers is proportional to the number of TOAs of the corresponding pulsar.

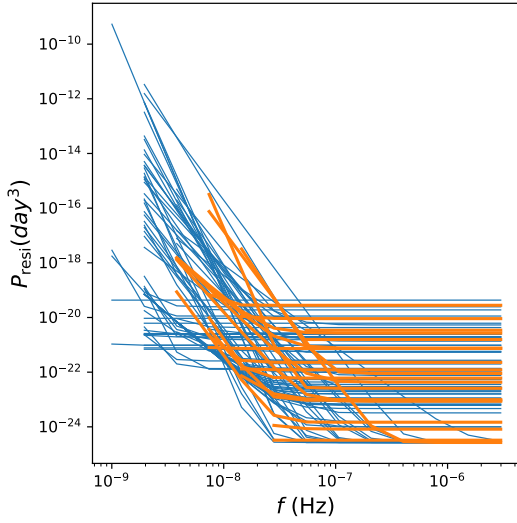


Fig. 14. The noise spectra of the pulsars. Blue curves correspond to known pulsars in existing PTAs, and orange curves are simulated new pulsars.

where θ , ι , Ψ are the angle between the direction towards the pulsar and the GW source, the inclination of the source binary plan and the polarization angle respectively. The SNR of the GW in the i -th pulsar is:

$$\rho_i^2 = \mathcal{A}_i^2 / S_{n,i}(f) \times T_i, \quad (43)$$

where $S_{n,i}(f)$ is the noise spectrum density of the pulsar, and T_i is the observation duration. The total SNR squared of a PTA is:

$$\rho^2 = \sum \rho_i^2. \quad (44)$$

The effects of a stochastic GW background (SGWB) to the timing residual are an additional red noise:

$$h_c^2(f) = C f^\gamma, \quad (45)$$

where h_c is the characteristic GW strain at the frequency 1 yr^{-1} , and the index γ depends on the origin of the SGWB. For incoherent overlapping of MBH, $\gamma = -2/3$; for relic GW, $\gamma = -1$ and

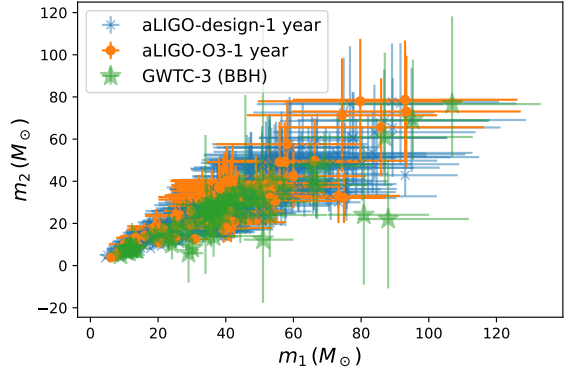
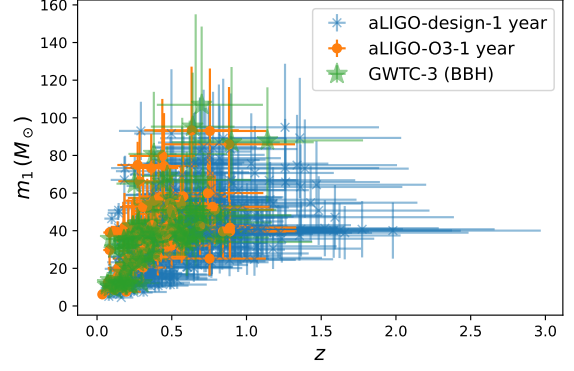


Fig. 15. aLIGO-design-1 year: The simulated catalogue from one year observation by aLIGO with designed noise performance on BBH, marked with blue crosses; **aLIGO-O3-1 year:** The simulated catalogue from one year observation by aLIGO with O3 noise performance on BBH, marked with orange dots; **GWTC-3 (BBH):** BBH events in GWTC-3, marked with green star symbols.

for cosmic strings, $\gamma = -7/6$. Besides the additional red noise, it is also expected that the timing residuals due to the SGWB are correlated between pairs of pulsars. The correlation as a function of the angular separation between the pair is:

$$\Gamma_0 = 3 \left\{ \frac{1}{3} + \frac{1 - \cos \xi}{2} \left[\ln \left(\frac{1 - \cos \xi}{2} - \frac{1}{6} \right) \right] \right\}, \quad (46)$$

which is referred as the Hellings and Downs Curve (Hellings & Downs 1983). The SNR squared in a pair of pulsars is (Anholm et al. 2009):

$$\rho_{1,2} = \frac{H_0^2}{4\pi^2} \sqrt{2T \int_0^\infty df \frac{\Omega_{\text{gw}}^2(f) \Gamma_0^2}{f^6 P_1(f) P_2(f)}}, \quad (47)$$

where H_0 is the Hubble constant, $\Omega_{\text{gw}}(f)$ is the energy density of the SGWB relative to the critical density of the Universe. The relation between $h_c(f)$ and $\Omega_{\text{gw}}(f)$ is:

$$h_c^2(f) = \frac{3H_0^2}{2\pi^2} \frac{1}{f^2} \Omega_{\text{gw}}(f). \quad (48)$$

In equation (47) $P_{1,2}(f) = S_{n1,2}(f) f^2$. The total SNR squared is the summation of SNR squared over all pairs in the PTA.

5. Results and examples

In order to test and validate the *GW-Toolbox*, we discuss the outcome of the simulations for the different source populations and different detectors, and compare these with the literature where possible.

5.1. Examples for stellar mass BBH detected with Earth-based detectors

For BBHs, we generate catalogues for a one year observation of aLIGO, both with the noise spectrum of O3 (aLIGO-O3) and that of the design (aLIGO-design). The underlying population model is BBH-PopB with the default parameters (delay time of 3 Gyr and a mass function with an extra Gaussian peak at $40M_{\odot}$, see section 3.1.1). The simulated number of detection of aLIGO-O3 is 99 (with a Poisson expectation 87.4). It is compatible with the rate of detection in O3a (~ 36 BBH in six month of observation with duty cycle $\sim 80\%$, see Abbott et al. (2020c)); the simulated number of detection for the aLIGO-design is 379 (expectation 376.0). In the panels of figure 15, we plot the simulated catalogues in the z - m_1 and m_1 - m_2 planes. To compare, we also plot the BBH events in GWTC-3 (Abbott et al. 2021b), which is comprised by GWTC-1 (Abbott et al. 2019b) and events detected in O3a+b. The simulated sets agree well with the observed ones, except that the uncertainties of parameters are in general larger in our simulation comparing with those in the real observation in GWTC-3 (up to $\sim 50\%$), especially in the low SNR region. The origin of this overestimation is double folded: 1, the intrinsic difference between FIM and Bayesian methods, as mentioned above; 2, the localisation information from triangulation is not included in our method as were in real catalogue. Therefore, the estimated uncertainties can serve as a conservative upper limits.

We also simulate a catalogue of one month observation with ET. In this case, the number of detection is 1923 (expectation 1.9×10^3). In the panels of figure 16, we plot the distribution of the catalogue in z and m_1 . We also plot the distribution of BBH mergers in the whole Universe as defined by the population model for comparison. From this example, it is clear that ET will probe the distribution of sources throughout the Universe very well, as was shown before (e.g. Vitale & Evans 2017). We will study this in more detail in a forthcoming paper (Yi et al. in preparation)

5.2. Examples for double neutron stars detected with Earth-based detectors

The number of DNS mergers detected so far is small (2-3). Therefore, we generate catalogues for ten years of detection of DNS mergers by aLIGO, both with the noise spectrum in O3 (aLIGO-O3) and that at design (aLIGO-design). The number of detection of aLIGO-O3 is 56 (expectation 48.7) in ten years, which is in accordance with the real detection rate in O3a (1-2 in six month); the number for aLIGO-design is 238 (expectation 236.3). In the panels of figure 17, we plot the simulated catalogues in the z - m_1 and m_1 - m_2 planes. We also plot the DNS events in GWTC-3 (GW170817, GW190425) to compare. It is difficult to draw strong conclusions with so few detection, but broadly the results of the *GW-Toolbox* agree with the observations so far. To look further in the future, we also simulate the catalogue of one year observation by ET. The expected number of detection is 168455 (expectation 1.68×10^5). In figure 18, we plot the distribution of the catalogue in redshifts and the total masses. We plot together

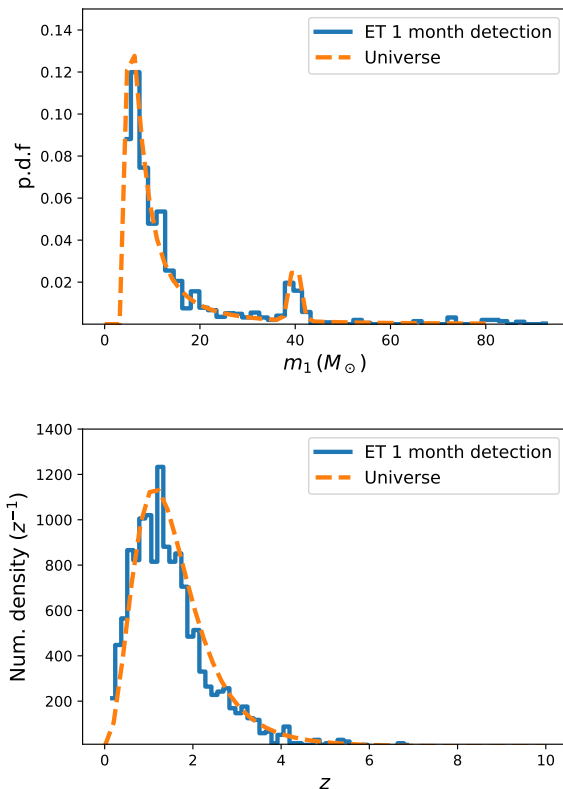


Fig. 16. m_1 distribution (upper panel) and the number density as function of redshift (lower panel) in the catalogue for one month of observation of BBH mergers by ET (solid blue). The integral of the latter is the total number of detection. As a comparison, we plot that of the whole Universe within one month in dashed orange.

the distribution of DNS mergers in the whole Universe as defined by the population model for comparison. As we can see from the upper panel of figure 18, the detected mass distribution is shifted to the high mass side, due to higher detectability; and in the lower panel of figure 18, we see the portion of detectable DNS merger decreases towards higher redshift, as expected.

5.3. Example for neutron star/black hole mergers detected with Earth-based detectors

In a similar way as above, we generate catalogues for ten years aLIGO observation for BHNS mergers, both with the noise spectrum in O3 (aLIGO-O3) and that at design (aLIGO-design). The underlying population model is BHNS-PopB with the default parameters. The event number in the simulated catalogue of aLIGO-O3 is 29 (a Poisson random with expectation value 32.0), which is compatible with the rate found in the O3 period (2-3 in one year); the number for aLIGO-design is 553 (expectation value 517.2). In the top and bottom panels of figure 19, we plot the simulated catalogues in z - m_{\bullet} and m_{\bullet} - m_n planes. A more sensitive detector would help to properly characterize this population.

We also simulate a catalogue for one year observation by ET. The number of events is 6251 (expectation 6.32×10^4). In the panels of figure 20, we plot the distribution of the catalogue in z , m_{\bullet} and m_n . We also plot the distribution of BHNS mergers in the whole Universe as defined by the population model for comparison. We see the effect that the fraction of detectable BHNS mergers increases towards higher masses, and decreases

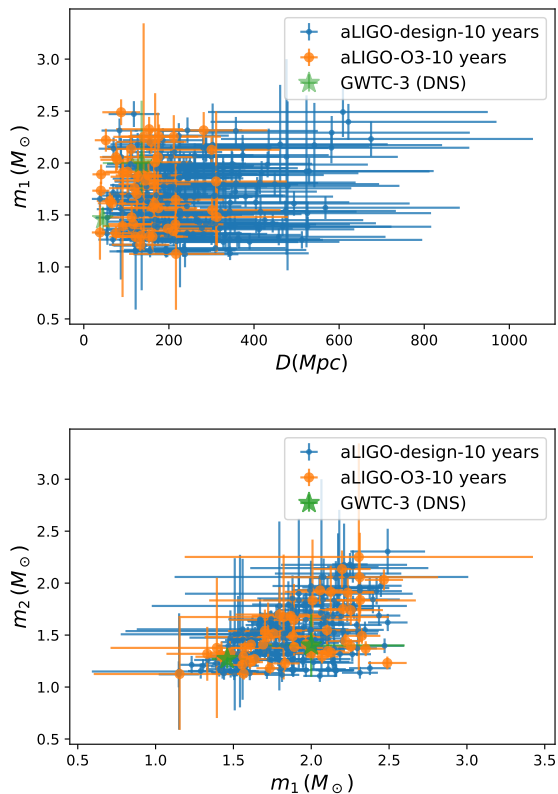


Fig. 17. The same as figure 15, but for ten years observation of DNS with eLIGO (design and O3 sensitivity).

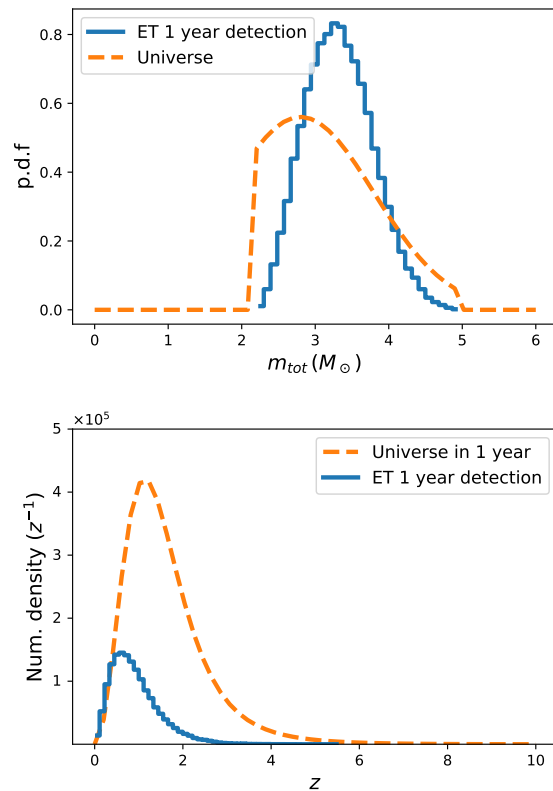


Fig. 18. The total mass distribution (upper panel) and the number density as function of red-shift (right panel) in the catalogue of one year observation of DNS mergers by ET (solid blue). The integral of the latter is the total number of detection. The dashed orange curve is that in the whole universe within one year.

towards higher redshift, although ET probes essentially the whole distribution.

5.4. Examples for SMBBH mergers detected with LISA

We now turn to the space-based detectors. The GW-Toolbox simulates the observed catalogue of SMBBH mergers by going through the catalogue in the Universe for a given observation duration, calculate the SNR for each SMBBH and select against the SNR cut-off, in this case $\text{SNR}=8$ as default. In figure 21, we plot the red-shifted chirp masses and the redshift of the total events and detected ones (squares on top of markers) by the standard LISA configuration in five years, corresponding to different population models. As we can see from figure 21, the detection horizon of our default LISA passes through the Pop3 population and below the Q3_delays and Q3_nodelays population. As a result, almost all events in Q3_delays and Q3_nodelays population are detectable, while the detectable fraction of Pop3 changes significantly with different LISA noise settings.

For these sources, we also calculate the uncertainties in the parameters. In panels of figure 22, we plot the distribution of the relative uncertainties of total masses, distances and sky localization $d\Omega$ in units of square degrees. The uncertainties are all estimated with a FIM method. The uncertainties span a wide range, but a significant fraction has quite well determined masses while only a small fraction has well determined distance and sky position. Our findings are in general in agree with previous results in Klein16.

5.5. Examples for DWDs detected with LISA

In order to simulate the DWDs observed by LISA, we go through a simulated catalogue of all Galactic DWDs and calculate their SNR with the analytic approximation in equation (37). Then we select the sources with SNR larger than the SNR threshold of 10 as the detected sources. We do the same for the verification binaries (VBs). In Table 3, we list the detected VBs and the estimated uncertainties of parameters. When calculating the uncertainties with FIM, the numerical waveform calculated with LDC are used. The results are compatible with earlier work, the SNR a bit lower than Kupfer et al. (2018), due the use of a slightly different LISA sensitivity. Since the size of the DWD catalogue is huge ($\sim 2.6 \times 10^7$), we go through a smaller sub-catalogue that are randomly drawn from the whole synthetic DWD catalogue instead, and scale the number of detection from this small sub-sample to the whole GWD catalogue to obtain the total expected number of detection. In figure 23, we plot the number of detection as function of the observation duration. Our results are about a factor of 0.5 lower than the earlier results e.g. in Nelemans et al. (2001); Nissanke et al. (2012); Korol et al. (2017). We attribute this to a slight difference in the LISA noise model or the DWD catalogue.

5.6. Examples for EMRIs detected with LISA

The signal from an EMRI can fall into the detectable frequency range of LISA from an early phase until the final plunge, which

Name	f (Hz)	β (deg)	λ (deg)	A	$d\Omega$ (deg ²)	SNR
J0806	$6.2 \times 10^{-3} \pm 3.1 \times 10^{-8}$	-4.704	120.442	$1.2 \times 10^{-22} \pm 6.5 \times 10^{-23}$	6.9×10^{-3}	91.851
V407 Vul	$3.5 \times 10^{-3} \pm 3.1 \times 10^{-8}$	46.783	294.995	$5.9 \times 10^{-23} \pm 1.1 \times 10^{-22}$	1.2×10^{-1}	65.930
ES Cet	$3.2 \times 10^{-3} \pm 3.1 \times 10^{-8}$	-20.334	24.612	$4.7 \times 10^{-22} \pm 1.0 \times 10^{-22}$	1.7×10^{-1}	46.347
ZTF J153932.16+502738.8	$4.8 \times 10^{-3} \pm 3.1 \times 10^{-8}$	66.162	205.031	$3.1 \times 10^{-24} \pm 1.8 \times 10^{-22}$	1.3×10^{-2}	188.051
SDSS J065133.34+284423.4	$2.6 \times 10^{-3} \pm 3.1 \times 10^{-8}$	5.805	101.340	$1.9 \times 10^{-23} \pm 1.6 \times 10^{-22}$	2.306	15.613
SDSS J093506.92+441107.0	$1.6 \times 10^{-3} \pm 3.1 \times 10^{-8}$	28.091	130.980	$7.6 \times 10^{-22} \pm 3.0 \times 10^{-22}$	19.776	10.653

Table 3. Detection of the verification binaries with the LISA detector.

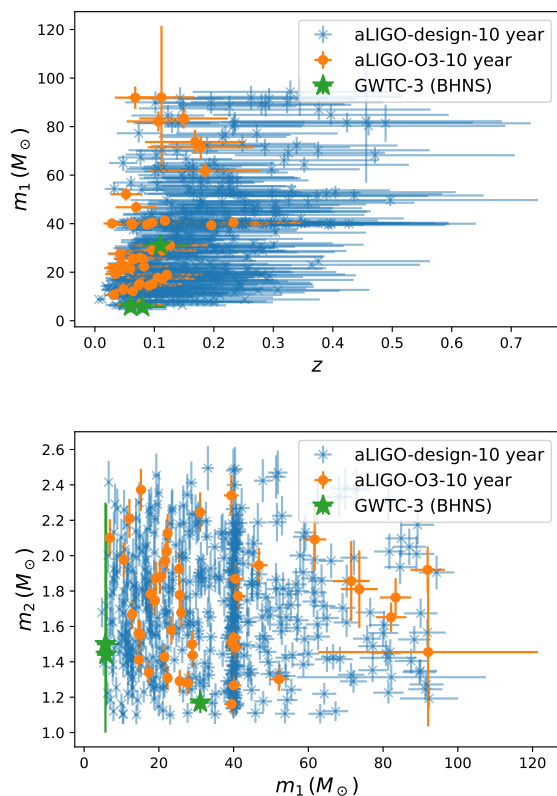


Fig. 19. **aLIGO-design-10 year:** The simulated catalogue from ten years’ observation by aLIGO with designed noise performance on BHNS, marked with blue crosses; **aLIGO-O3-10 year:** The simulated catalogue from ten year observation by aLIGO with O3 noise performance on BHNS, marked with orange dots.

can span quite a long duration from months to years. In order to guarantee the speed of simulation, we use a frequency domain waveform (modulus) generated in advance and stored in files. In each simulation, we go through all the candidate events in the catalogue, read in the corresponding TDI waveform modulus and calculate the SNR against the noise curve. The detected events are then selected against an SNR-threshold. In the EMRIs catalogues that we are using, there are also pre-calculated SNR for each system, which corresponds to a slightly different LISA setup and waveform (see Babak17). In figure 24, we compare their pre-calculated SNRs with ours of the same catalogue for one year observation of the M1 population with our default LISA. Our calculated SNR values disperse within a factor two around the values of Babak17. We attribute this dispersion to the slightly different LISA noise and waveform (AK Schwarzschild versus AK Kerr, see Babak17). In figure 25, we plot the histogram of the SNR of the bright EMRIs in the catalogue of Babak17 and

that calculated from this work. The underlying population model is M1. In panels of figure 26, we plot histograms of relative uncertainties of the masses μ , M , distance D and sky location Ω (in units of square degrees) in a catalogue detected by the default LISA. The observation duration is two years, and the SNR cut-off is set to 20 and the population is M1. The uncertainties are estimated with FIM (section 4.1.2). In the calculation of FIM, derivatives of the complex waveform relative to all the relevant parameters are needed (equation 23). Therefore, if we were to use the pre-calculated waveform for the uncertainty estimation, the storing files would be ~ 20 times larger in size than those used for the SNR calculation. On that account, we calculate the late stage waveform in real time and use them for the uncertainty evaluation. In general the parameters of EMRIs are very well determined, except in some cases the sky position. The estimated level of uncertainties are in agreement with Babak17.

5.6.1. Results for PTAs

For PTAs, we calculate the detection limits for individual SMBBHs and a stochastic background based on the different PTA configurations. Given a certain PTA, a SNR cut-off and the coordinates of the source, we can give a sensitivity curve for GW emitted by an individual SMBBH, as a function of frequency. In figure 27, we plot the sky-averaged sensitivity curve to individual sources of EPTA, PPTA, NANOGrav, IPTA and a simulated future PTA (labeled “future”). For the future PTA, we assume daily observation on the IPTA pulsars for 10 more years, with two more new pulsars being added to the PTA per year (the setting of the future PTA can be customized by users). The corresponding $\rho_{\text{cri}} = 10$. The results are in agreement with published ones (Babak et al. 2016; Schutz & Ma 2016; Aggarwal et al. 2019).

In Table 4, we list the upper limits on the SGWB of different origins, the corresponding $\rho_{\text{cri}} = 100$. They are broadly in agreement with published results (to within a factor ~ 2), which are also listed in the table in the parentheses.

6. Caveats & Discussion

We have implemented and described a first version of the GW-Toolbox, which still has a few caveats and is missing some ingredients that we plan to implement in the (near) future. The most important caveats of the current version are:

- Higher order multipole modes of the waveform: Theoretically, GW radiation are treated with spin-weighted spherical decomposition (Thorne 1980). The leading term is the $\ell = 2$, $|m| = 2$ (quadrupole) term. In the current GW-Toolbox, we apply a waveform that neglects the higher order modes beyond quadrupole. High order modes will extend the spectrum of a

	SBHBH ($A_{\text{yr}^{-1}}$)	Cosmic Strings ($\Omega_{\text{gw, yr}^{-1}} h^2$)	Relic ($\Omega_{\text{gw, yr}^{-1}} h^2$)
EPTA (Lentati et al. 2015)	$1.4 \times 10^{-15} (3 \times 10^{-15})$	2.5×10^{-10}	$4.7 \times 10^{-10} (1.2 \times 10^{-9})$
PPTA (Shannon et al. 2015)	$2.45 \times 10^{-15} (1 \times 10^{-15})$	6.4×10^{-10}	1.2×10^{-9}
NANOGrav (Arzoumanian et al. 2018)	$1.6 \times 10^{-15} (1.45 \times 10^{-15})$	3.6×10^{-10}	$6.3 \times 10^{-10} (3.4 \times 10^{-10})$
IPTA	9.9×10^{-16}	1.0×10^{-10}	2.0×10^{-10}

Table 4. The upper limits set with different PTAs to SGWB of different origins, $\rho_{\text{cri}} = 100$. Numbers in parentheses are values in literature. The most recent reported upper limit on the GW originates from Cosmic String are in terms of the cosmic-string tension ($G\mu$). The conversion from $G\mu$ to $\Omega_{\text{gw, yr}^{-1}} h^2$ depends on models and the reconnection probability p , so we cannot give literature values.

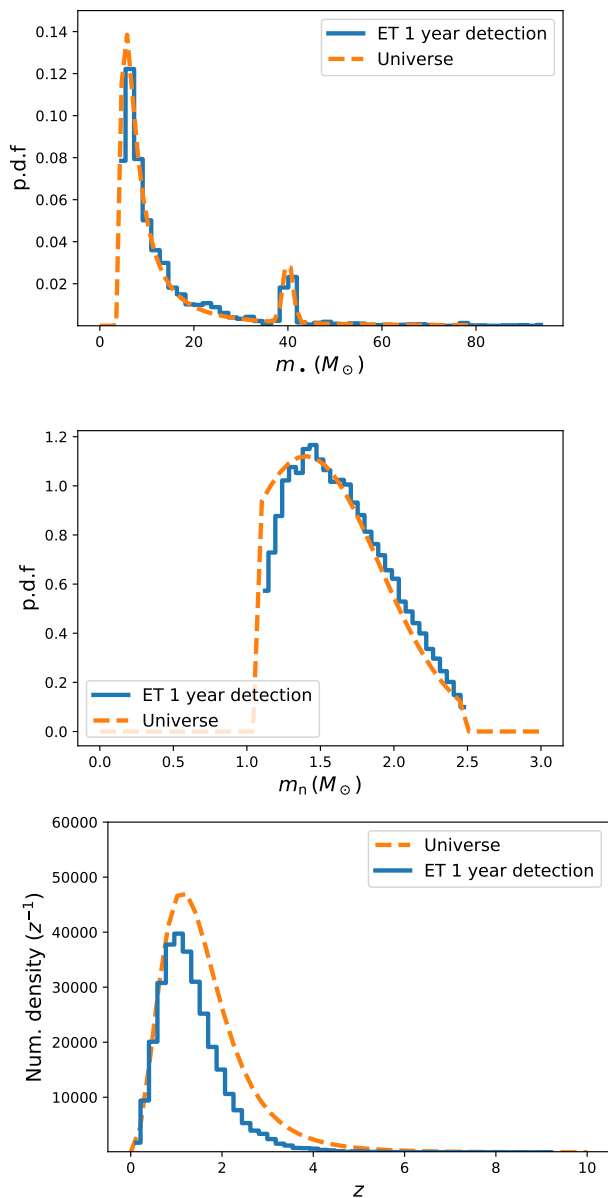


Fig. 20. The Probability density distribution as function of m_\bullet (upper panel), m_n (middle panel) and the number density as function of red-shift (lower panel) for 10 years observation of BHNS mergers by ET. The integral of the latter is the total number of detection. The orange lines show the intrinsic distributions.

GW to high frequencies (London et al. 2018), and their significance increase with higher mass inequality, higher total mass and higher orbital inclination angle (Mills & Fairhurst 2021). Including higher order modes in the waveform can break the

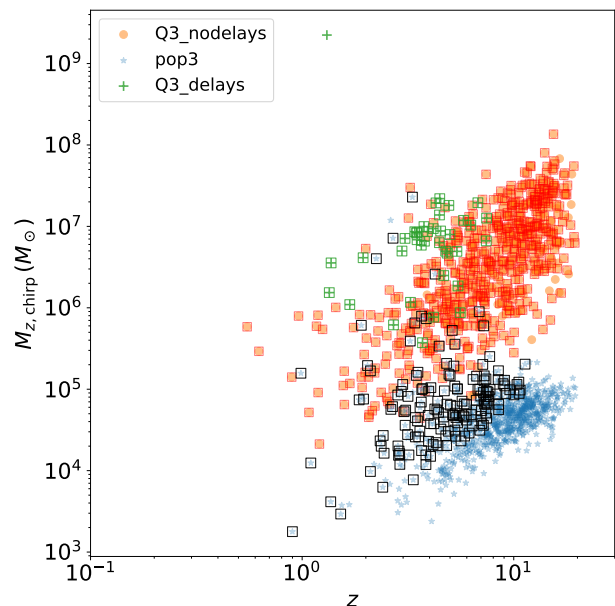


Fig. 21. The red-shifted chirp masses and the redshift of the total events (markers) and detected ones (squares on top of markers) by the standard LISA configuration in five years. Orange, blue and green markers correspond to Q3_nodelay, pop3 and Q3_delays population models respectively. The underlying SNR cutoff is 8.

degeneracy between the inclination angle and the distance, thus results in more accurate estimate of the parameters of the source (London et al. 2018). In the O3 observation, there are already some GW events with evidence of higher order modes (GW170729: Chatziioannou et al. 2019; GW190412: Abbott et al. 2020b; GW190814: Abbott et al. 2020d). Mills & Fairhurst (2021) found that a few percent of binaries will be detected with higher order modes by aLIGO with designed sensitivity. For 3G GW detectors, Divyajyoti et al. (2021) found that the SNR contribution from higher order modes in some GWTC-3 systems would surpass 10% of the total SNR. For larger total mass and mass ratio binaries, the higher order modes are expecting to contribute a significant fraction of the SNR. Therefore, neglecting higher order modes in the waveform will result in an underestimate of the detection rate of sources, especially for those with large total mass and mass ratio. In an updated GW-Toolbox, the waveform will be replaced with one that includes the higher order modes, e.g., PhenomHM (London et al. 2018).

- Uncertainties estimation for Earth-based detectors: the uncertainties are estimated in a hybrid way: those of the intrinsic parameters ($m_{i,z}$ and χ) are calculated with FIM, with all of the amplitude parameters treated as one. In addition, the uncertainty on the red-shift (δz) is estimated with empirical relations. Then the source-frame masses uncertainties are cal-

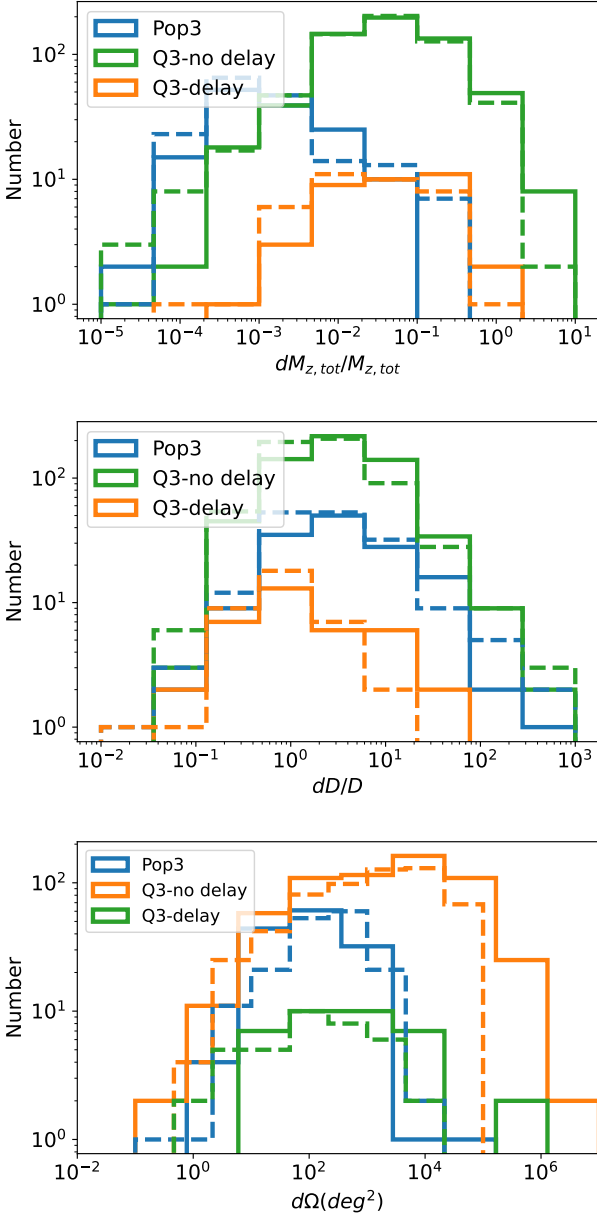


Fig. 22. **Upper:** The distribution of relative uncertainties on the total masses in the catalogue of MBH mergers detected by LISA in five year. Solid lines are for default LISA and dashed lines are for 5Gm arm length; **Middle** Same as the upper panel, but on the relative uncertainties on the luminosity distances; **Lower:** Same as the upper two panels, but on uncertainties of the sky location (deg^2).

culated with error propagation equation (Equation 24). Equation (24) is valid only when the covariance between $dm_{i,z}$ and dz is vanishing. Since $m_{i,z}$ are largely determined from matching the phases of the waveform, while the constraint on z comes from the fitting amplitude of the waveform, we expect that the dependence between $dm_{i,z}$ and dz are weak. A more self-consistent and accurate non-Bayesian treatment would be: to treat all extrinsic parameters separately in the FIM (the dimensional of FIM will thus be enlarged), and calculate the covariance among all parameters explicitly. Then impose the constraints from the triangulation localization and obtain the uncertainties on all parameters.

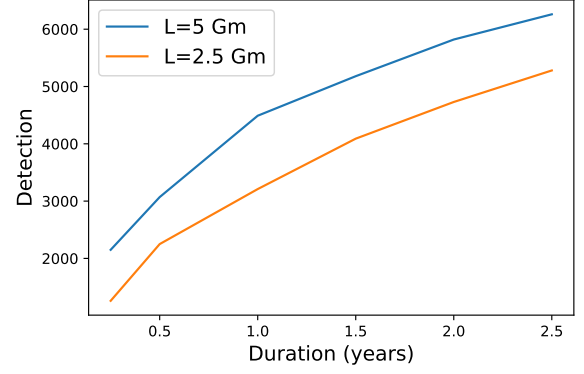


Fig. 23. The detected number of DWDs with the default LISA and a larger LISA with 5 million km arms as function of the observation duration. We use a threshold SNR $\rho_* = 7$

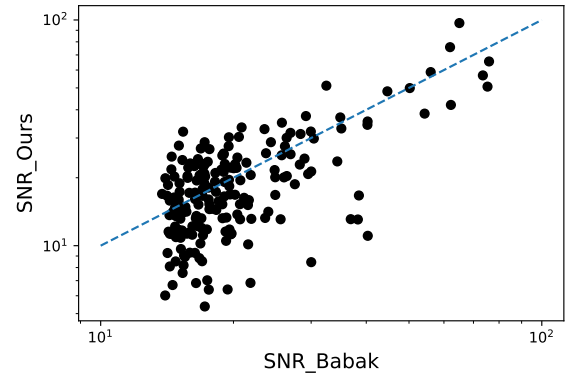


Fig. 24. The pre-calculated SNR by Babak17 comparing with SNR of this work for the same catalogue, for one years' observation on M1 population.

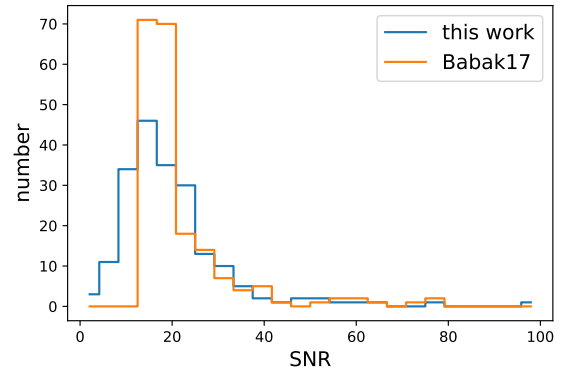


Fig. 25. Histogram of the SNR of the bright EMRIs in catalogue of Babak17. The blue histogram indicate the SNR calculated in this work, and the orange histogram is that pre-calculated by Babak17 using a slightly different LISA noise and waveform.

- Populations and Waveforms of EMRIs: In order to return the simulated catalogue of detection in a tolerable time for a website user, we use catalogues of EMRIs in which only bright ones are included (pre-calculated $\text{SNR}_{\text{tot}} > 20$). Therefore, the user should not set an SNR cut-off lower than ~ 15 , otherwise the returned synthetic catalogue is incomplete. In order

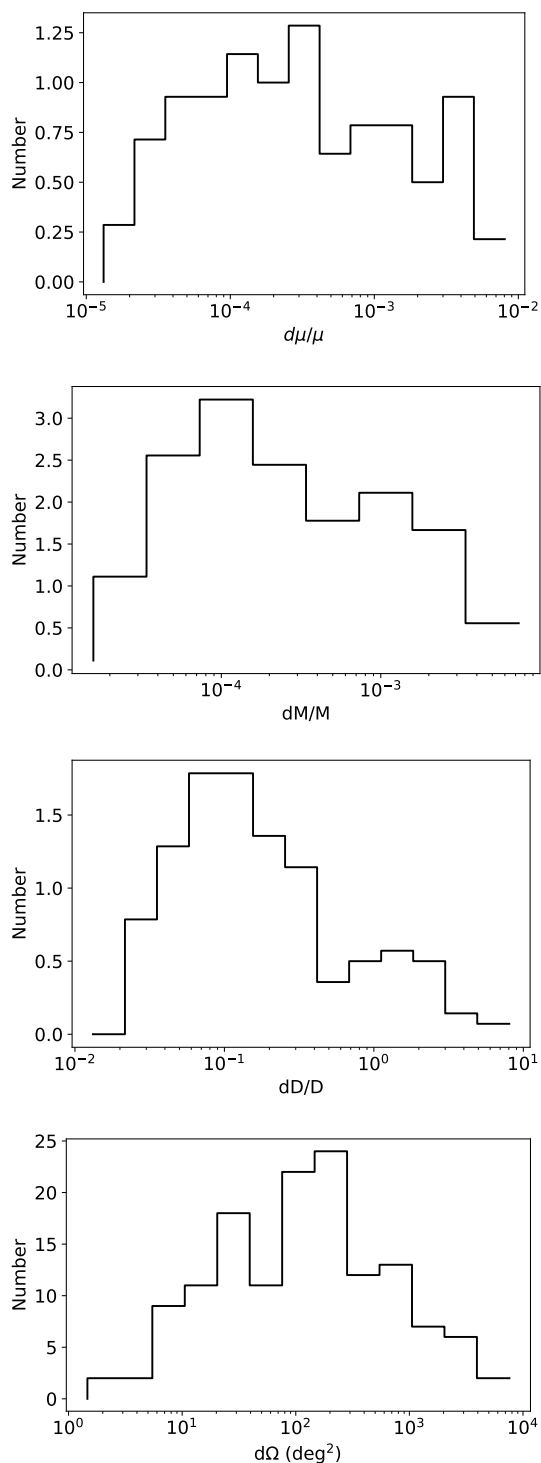


Fig. 26. Histogram of relative uncertainties on the mass of the lighter component μ , the mass of the heavier component M , the distance D and the uncertainties of the sky location $d\Omega$ in a catalogue of EMRIs detected by the default LISA for a two year observation. The SNR cut-off is set to 20.

to compare with previous results of Babak17, the waveform we employed is analytic kludge, which is known to be fast but less realistic. In the `GW-Toolbox`, it can be replaced with a more accurate waveform augmented analytic kludge (AAK) easily, since the latter can also be simulated with the same package `EMRI_Kludge_Suite`. For the sake of the speed of

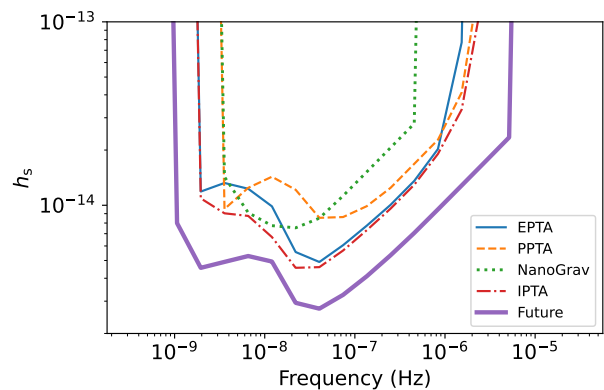


Fig. 27. Sensitivity plot for an individual SMBBH as function of frequency, for $\rho_{\text{cri}} = 10$ and averaged over the celestial sphere for different PTAs.

simulation, we use the pre-calculated frequency domain TDI waveform for the SNR calculation. When estimating the uncertainties using FIM methods of the detected sources, we only include the late stage of their waveform. As shown in the above sections, we will miss some of the low frequency section corresponding to the early inspiral stage, which is in fact detectable by LISA, and results in underestimation of the accuracy of parameters inference. As shown in examples in the above section, such underestimation is not severe.

- PTAs: Our sensitivity curves and upper limits are given according to an SNR threshold and the SNR of GW are calculated based on a simplified parameterised noise spectra. On the other hand, upper limits are reported in literature with confidence levels. Due to the very different nature between the methods, the correspondence between the confidence level in literature and our SNR threshold is difficult to explore. In our examples, we set the $\rho_{\text{cri}} = 10$ for continuous GW in plotting the sensitivity curves, and $\rho_{\text{cri}} = 100$ for SGWB, in order to obtain results which are in order of magnitude in accordance with literature. For continuous GW, the sensitivity scales with the ρ_{cri} ; while for SGWB, upper limits on the characteristic strain scale with the square root of ρ_{cri} .

We plan to include a number of additions to the `GW-Toolbox` in the future. The first ones involve several proposed space-borne detectors, in particular DECIGO, Taiji and Tianqin. In the ground-based and space-borne modules, we will integrate SNR calculators for individual sources that are specified by the user. On a longer time scale, we plan to include more GW sources, *e.g.*, supernovae explosions, single spinning and recycling neutron stars, multiple black holes encounters and catalogs of SMBBH for PTAs. We are also working to extend the `GW-Toolbox` with electro-magnetic counterparts, *e.g.*, to return the fluence of short GRBs and peak fluxes of kilonovae. Triangulation of a network of ground-based detectors will also be developed.

In the next step, the `GW-Toolbox` will have the ability to simulate observations of different evolutionary phases of the same population in different GW frequency ranges. For instance, each population of compact object mergers corresponds to a population of persistent GW source from the earlier phase. The former are targets of ground-based interferometers, while the latter are targets of space-borne interferometers. Another instance is the close orbit and inspiral-merger phases of SMBBH, which can be observed with PTA and LISA respectively. We will also in-

clude simulated observation on SGWB with ground-based and LISA-like detectors.

7. summary

In this paper, we introduce the `GW-Toolbox` (www.gw-universe.org), a set of tools that quickly simulates a Universe with kHz/mHz/nHz GW source populations, and observations with different GW detectors, i.e., ground-based interferometers, space-borne interferometers and pulsar timing arrays. We hereby summarize the functionalities and methodologies of the `GW-Toolbox` for each module:

- The module for ground-based interferometers simulates observation of mergers of compact objects, including binary black holes (BBH), double neutron stars (DNS) and black hole-neutron stars (BHNS). The detectors include default aLIGO, Virgo, KAGRA, Einstein Telescope and Cosmic Explorer, and a user customised LIGO/Virgo-like and ET-like detectors. The noise curves of the default detectors are taken from the literature, and those of user customised detectors are simulated with the `FINESSE` software. After the noise curve and antenna patterns are determined, we calculate the optimal SNR for all sources in the selected source class. A simplified `IMRPhenomD` waveform that assumes zero effective spin is employed in this step. With a certain SNR-threshold of detection, we marginalize the geometrical parameters and obtain the detectability $\mathcal{D}(m_1, m_2, z, \chi)$ as function of the source's masses, redshift (luminosity distance) and effective spin. The product of $\mathcal{D}(m_1, m_2, z, \chi)$ and the user-selected probability density function (p.d.f) of the source population defines the p.d.f of the detectable sources, $N_d(m_1, m_2, z, \chi)$. A synthetic catalogue of observations is obtained with a MCMC sampling from the $N_d(m_1, m_2, z, \chi)$. We use Fisher Information Matrix (FIM) method to estimate the uncertainties of the parameters of events. In the process of calculating the FIM, we apply the complete `IMRPhenomD` waveform phases (for aligned spins).
- The module for space-borne interferometers simulates observations with LISA or a customised LISA-like configuration. The noise power density in the `TDI-X` response channel is calculated with an analytical formula, which includes acceleration noise, laser shot noise, other optical Meteorology noises and confusion noise due to Galactic double white dwarf (DWD) foreground. The targets we include are the inspiral of Supermassive Binary Black Holes (SMBBH), individual resolvable Galactic DWD and Extreme Mass Ratio Inspirals (EMRIs). For SMBBH, we calculate the `TDI-X` LISA responses of a GW source with LDC codes. The optimal SNR is subsequently calculated. There are three population models being considered, namely `Pop3`, `Q3_nodeLays` and `Q3_delays`, taken from Babak17. There are ten realizations of the simulated catalogues of SMBBH mergers in the Universe within five years for each population model. The `GW-Toolbox` will re-sample from the catalogue according to user specified observation duration, and calculate the SNR for each source in the sample. A synthetic detection catalogue is thus returned based on a SNR threshold of detection set by the user. The uncertainties are estimated with FIM. For DWDs, we use an analytic equation to calculate the modulus `TDI-X` LISA response to a series of sinusoidal GWs, and therefore the SNR. We consider two samples of DWDs, namely the verification DWDs and a simulated entire Galactic population. For the former sample, the SNR is calculated individually in the catalogue, and a detected catalogue is returned according

to a SNR threshold. For the latter sample, due to its huge number, we randomly draw a sub-sample from it, and find the catalogue of detections in the sub-sample. The total expected number of detection is obtained by rescaling the number of events in the returned catalogue. The uncertainties are also estimated with FIM, where we use LDC codes for the complex `TDI` LISA response, instead of using the analytical equation as in the SNR computation. For EMRIs, we make use of the `EMRI_Kludge_Suite` for the `TDI` LISA response, and therefore the SNR. We calculate the SNR for each source in pre-simulated catalogues of EMRIs of different populations, and select those with SNR surpassing the SNR threshold. The uncertainties are again computed with FIM.

- In the PTA module, we include four currently operating PTAs: EPTA, PPTA, NANOGrav and IPTA. For the pulsars in these PTAs, we use the following parameters to represent their noises properties and observation campaigns: the levels of white noise, the level of red noise, the red noise spectrum index, total observation duration and averaged interval between observations. We allow users to include new pulsars which will be discovered in the course of future observations. The sky-locations of the new pulsars and their noise properties are randomly assigned according to the distributions of those of the known pulsars. In this module, the `GW-Toolbox` computes the SNR of a series of monochromatic GWs with given frequency and amplitude, which corresponds to a GW from the orbital motion of SMBBH. Another function of this module is to evaluate the upper limit that a PTA can set to Stochastic GW Background (SGWB) from different origins.

In the (near) future, the `GW-Toolbox` will be extended with new standard detectors, triangulation of a network of ground-based detectors, new source classes and electro-magnetic counterparts and the ability to "observe" the same source model with different detectors. In this way, the `GW-Toolbox` will provide even more functionality to give users quick idea of the power of different GW detectors for their favourite source population.

Acknowledgements

We thank the many researchers that provided results for the different source populations and detectors that made it possible to collect all these together in the `GW-Toolbox`. We also thank the referee for comments and detailed testing that greatly improved the paper and the `GW-Toolbox`. We thank in particular the (Mock) LISA Data Challenge team and the participating groups that made it possible to include so many results in the space module. Special thanks to Stas Babak and Antoine Petiteau for help and support. We thank our colleagues Paul Groot, Samaya Nissanke, Sarah Caudill, Chris van den Broeck, Gemma Janssen, Antonia Rowlinson, Peter Jonker, Selma de Mink, Marc Klein-Wolt and Jess Broderick for the initial discussions that led to this project. This research was made possible by support from the Dutch National Science Agenda, NWA Startimpuls – 400.17.608

References

- Abbott, B. P., Abbott, R., Abbott, T. D., et al. 2016, *Phys. Rev. Lett.*, 116, 061102. doi:10.1103/PhysRevLett.116.061102
- Abbott, B. P., Abbott, R., Abbott, T. D., et al. 2016, *ApJ*, 818, L22. doi:10.3847/2041-8205/818/2/L22
- Abbott, B. P., Abbott, R., Abbott, T. D., et al. 2017, *Phys. Rev. Lett.*, 119, 161101. doi:10.1103/PhysRevLett.119.161101
- Abbott, B. P., Abbott, R., Abbott, T. D., et al. 2017, *ApJ*, 848, L12. doi:10.3847/2041-8213/aa91c9

- Abbott, B. P., Abbott, R., Abbott, T. D., et al. 2017, *ApJ*, 848, L13. doi:10.3847/2041-8213/aa920c
- Abbott, B. P., Abbott, R., Abbott, T. D., et al. 2017, *Nature*, 551, 85. doi:10.1038/nature24471
- Abbott, B. P., Abbott, R., Abbott, T. D., et al. 2017, *ApJ*, 850, L39. doi:10.3847/2041-8213/aa9478
- Abbott, B. P., Abbott, R., Abbott, T. D., et al. 2017, *ApJ*, 850, L40. doi:10.3847/2041-8213/aa93fc
- Abbott, B. P., Abbott, R., Abbott, T. D., et al. 2018, *Phys. Rev. Lett.*, 121, 161101. doi:10.1103/PhysRevLett.121.161101
- Abbott, B. P., Abbott, R., Abbott, T. D., et al. 2018, *Phys. Rev. Lett.*, 120, 091101. doi:10.1103/PhysRevLett.120.091101
- Abbott, B. P., Abbott, R., Abbott, T. D., et al. 2019, *Physical Review X*, 9, 011001. doi:10.1103/PhysRevX.9.011001
- Abbott, B. P., Abbott, R., Abbott, T. D., et al. 2019, *Physical Review X*, 9, 031040. doi:10.1103/PhysRevX.9.031040
- Abbott, B. P., Abbott, R., Abbott, T. D., et al. 2019, *Phys. Rev. Lett.*, 122, 061104. doi:10.1103/PhysRevLett.122.061104
- Abbott, B. P., Abbott, R., Abbott, T. D., et al. 2019, *Phys. Rev. Lett.*, 123, 011102. doi:10.1103/PhysRevLett.123.011102
- Abbott, B. P., Abbott, R., Abbott, T. D., et al. 2019, *ApJ*, 882, L24. doi:10.3847/2041-8213/ab3800
- Abbott, B. P., Abbott, R., Abbott, T. D., et al. 2020, *Classical and Quantum Gravity*, 37, 045006. doi:10.1088/1361-6382/ab5f7c
- Abbott, R., Abbott, T. D., Abraham, S., et al. 2020, *Phys. Rev. D*, 102, 043015. doi:10.1103/PhysRevD.102.043015
- Abbott, R., Abbott, T. D., Abraham, S., et al. 2020, [arXiv:2010.14527](https://arxiv.org/abs/2010.14527)
- Abbott, R., Abbott, T. D., Abraham, S., et al. 2020, *ApJ*, 896, L44. doi:10.3847/2041-8213/ab960f
- Abbott, R., Abbott, T. D., Abraham, S., et al. 2021, *ApJ*, 915, L5. doi:10.3847/2041-8213/ac082e
- Abbott, R., Abbott, T. D., Acernese, F., et al. 2021, link: https://dcc.ligo.org/public/0170/P2000318/007/o3b_catalog.pdf
- Acernese, F., Agathos, M., Agatsuma, K., et al. 2015, *Classical and Quantum Gravity*, 32, 024001. doi:10.1088/0264-9381/32/2/024001
- Aggarwal, N., Aguiar, O. D., Bauswein, A., et al. 2020, [arXiv:2011.12414](https://arxiv.org/abs/2011.12414)
- Aggarwal, K., Arzumianian, Z., Baker, P. T., et al. 2019, *ApJ*, 880, 116. doi:10.3847/1538-4357/ab2236
- Aggarwal, K., Arzumianian, Z., Baker, P. T., et al. 2020, *ApJ*, 889, 38. doi:10.3847/1538-4357/ab6083
- Alam, M. F., Arzumianian, Z., Baker, P. T., et al. 2020, [arXiv:2005.06495](https://arxiv.org/abs/2005.06495)
- Armstrong, J. W., Estabrook, F. B., & Tinto, M. 1999, *ApJ*, 527, 814
- Amaro-Seoane, P., Gair, J. R., Freitag, M., et al. 2007, *Classical and Quantum Gravity*, 24, R113. doi:10.1088/0264-9381/24/17/R01
- Amaro-Seoane, P., Audley, H., Babak, S., et al. 2017, [arXiv:1702.00786](https://arxiv.org/abs/1702.00786)
- Anholm, M., Ballmer, S., Creighton, J. D. E., et al. 2009, *Phys. Rev. D*, 79, 084030. doi:10.1103/PhysRevD.79.084030
- Arzumianian, Z., Baker, P. T., Brazier, A., et al. 2018, *ApJ*, 859, 47. doi:10.3847/1538-4357/aabd3b
- Ajith, P., Hannam, M., Husa, S., et al. 2011, *Phys. Rev. Lett.*, 106, 241101
- Arzumianian, Z., Baker, P. T., Blumer, H., et al. 2020, *ApJ*, 905, L34. doi:10.3847/2041-8213/abd401
- Astropy Collaboration, Robitaille, T. P., Tollerud, E. J., et al. 2013, *A&A*, 558, A33. doi:10.1051/0004-6361/201322068
- Astropy Collaboration, Price-Whelan, A. M., Sipőcz, B. M., et al. 2018, *AJ*, 156, 123. doi:10.3847/1538-3881/aabc4f
- Barack, L. & Cutler, C. 2004, *PRD*, 69, 082005
- Barke, S., Wang, Y., Esteban Delgado, J. J., et al. 2015, *Classical and Quantum Gravity*, 32, 095004. doi:10.1088/0264-9381/32/9/095004
- Babak, S., Baker, J. G., Benacquista, M. J., et al. 2010, *Classical and Quantum Gravity*, 27, 084009. doi:10.1088/0264-9381/27/8/084009
- Babak, S. & Sesana, A. 2012, *Phys. Rev. D*, 85, 044034. doi:10.1103/PhysRevD.85.044034
- Babak, S., Petiteau, A., Sesana, A., et al. 2016, *MNRAS*, 455, 1665. doi:10.1093/mnras/stv2092
- Babak, S., Gair, J., Sesana, A., et al. 2017, *Phys. Rev. D*, 95, 103012. doi:10.1103/PhysRevD.95.103012
- Barausse, E. 2012, *MNRAS*, 423, 2533. doi:10.1111/j.1365-2966.2012.21057.x
- Barausse, E., Berti, E., Hertog, T., et al. 2020, *General Relativity and Gravitation*, 52, 81. doi:10.1007/s10714-020-02691-1
- Belczynski, K., Kalogera, V., & Bulik, T. 2002, *ApJ*, 572, 407. doi:10.1086/340304
- Belczynski, K., Holz, D. E., Bulik, T., et al. 2016, *Nature*, 534, 512. doi:10.1038/nature18322
- Berti, E., Cardoso, V., & Will, C. M. 2006, *Phys. Rev. D*, 73, 064030. doi:10.1103/PhysRevD.73.064030
- Brown, D. D., Jones, P., Rowlinson, S., et al. 2020, *SoftwareX*, 12, 100613. doi:10.1016/j.softx.2020.100613
- Burke-Spolaor, S., Taylor, S. R., Charisi, M., et al. 2019, *A&A Rev.*, 27, 5. doi:10.1007/s00159-019-0115-7
- Caprini, C. & Figueroa, D. G. 2018, *Classical and Quantum Gravity*, 35, 163001. doi:10.1088/1361-6382/aac608
- Chatziioannou, K., Costeta, R., Ghonge, S., et al. 2019, *Phys. Rev. D*, 100, 104015. doi:10.1103/PhysRevD.100.104015
- Chruslińska, M., Nelemans, G., & Belczynski, K. 2019, *MNRAS*, 482, 5012. doi:10.1093/mnras/sty3087
- Chruslińska, M., Jędrabková, T., Nelemans, G., et al. 2020, *A&A*, 636, A10. doi:10.1051/0004-6361/202037688
- Chua, A. J. K. & Gair, J. R. 2015, *Classical and Quantum Gravity*, 32, 232002. doi:10.1088/0264-9381/32/23/232002
- Chua, A. J. K., Moore, C. J., & Gair, J. R. 2017, *Phys. Rev. D*, 96, 044005. doi:10.1103/PhysRevD.96.044005
- Clark, J. P. A., van den Heuvel, E. P. J., & Sutantyo, W. 1979, *A&A*, 72, 120
- Colpi, M. 2014, *Space Sci. Rev.*, 183, 189. doi:10.1007/s11214-014-0067-1
- Cornish, N. J. & Littenberg, T. B. 2007, *Phys. Rev. D*, 76, 083006. doi:10.1103/PhysRevD.76.083006
- Coulter, D. A., Foley, R. J., Kilpatrick, C. D., et al. 2017, *Science*, 358, 1556. doi:10.1126/science.aap9811
- Dahal, P. K. 2020, *Journal of Astrophysics and Astronomy*, 41, 8. doi:10.1007/s12036-020-9625-y
- Damour, T. & Vilenkin, A. 2001, *Phys. Rev. D*, 64, 064008. doi:10.1103/PhysRevD.64.064008
- Damour, T. & Vilenkin, A. 2005, *Phys. Rev. D*, 71, 063510. doi:10.1103/PhysRevD.71.063510
- Demorest, P. B., Ferdman, R. D., Gonzalez, M. E., et al. 2013, *ApJ*, 762, 94. doi:10.1088/0004-637X/762/2/94
- Desvignes, G., Caballero, R. N., Lentati, L., et al. 2016, *MNRAS*, 458, 3341. doi:10.1093/mnras/stw483
- Detweiler, S. 1979, *ApJ*, 234, 1100. doi:10.1086/157593
- de Mink, S. E. & Belczynski, K. 2015, *ApJ*, 814, 58. doi:10.1088/0004-637X/814/1/58
- Divyjayoti, Baxi, P., Mishra, C. K., et al. 2021, *Phys. Rev. D*, 104, 084080. doi:10.1103/PhysRevD.104.084080
- Dominik, M., Berti, E., O'Shaughnessy, R., et al. 2015, *ApJ*, 806, 263. doi:10.1088/0004-637X/806/2/263
- Ellis, J. A., Siemens, X., & Creighton, J. D. E. 2012, *ApJ*, 756, 175. doi:10.1088/0004-637X/756/2/175
- Ellis, J. A. 2013, *Classical and Quantum Gravity*, 30, 224004. doi:10.1088/0264-9381/30/22/224004
- Estabrook, F. B., Tinto, M., & Armstrong, J. W. 2000, *Phys. Rev. D*, 62, 042002
- Farr, W. M., Sravan, N., Cantrell, A., et al. 2011, *ApJ*, 741, 103. doi:10.1088/0004-637X/741/2/103
- Farrow, N., Zhu, X.-J., & Thrane, E. 2019, *ApJ*, 876, 18. doi:10.3847/1538-4357/ab12e3
- Ferrarese, L. & Merritt, D. 2000, *ApJ*, 539, L9. doi:10.1086/312838
- Fryer, C. L. & Kalogera, V. 2001, *ApJ*, 554, 548. doi:10.1086/321359
- Gair, J. R., Barack, L., Creighton, T., et al. 2004, *Classical and Quantum Gravity*, 21, S1595. doi:10.1088/0264-9381/21/20/003
- Goetz, E. & Riles, K. 2011, *Classical and Quantum Gravity*, 28, 215006. doi:10.1088/0264-9381/28/21/215006
- González, G., Viceré, A., & Wen, L. 2013, *Frontiers of Physics*, 8, 771. doi:10.1007/s11467-013-0329-5
- Grishchuk, L. P. 1976, *Soviet Journal of Experimental and Theoretical Physics Letters*, 23, 293
- Grishchuk, L. P. 1977, *Eighth Texas Symposium on Relativistic Astrophysics*, 302, 439. doi:10.1111/j.1749-6632.1977.tb37064.x
- Harry, G. M. & LIGO Scientific Collaboration 2010, *Classical and Quantum Gravity*, 27, 084006. doi:10.1088/0264-9381/27/8/084006
- Hellings, R. W. & Downs, G. S. 1983, *ApJ*, 265, L39. doi:10.1086/183954
- Hild, S., Chelkowski, S., & Freise, A. 2008, [arXiv:0810.0604](https://arxiv.org/abs/0810.0604)
- Hild, S., Chelkowski, S., Freise, A., et al. 2010, *Classical and Quantum Gravity*, 27, 015003. doi:10.1088/0264-9381/27/1/015003
- Hild, S., Abernathy, M., Acernese, F., et al. 2011, *Classical and Quantum Gravity*, 28, 094013. doi:10.1088/0264-9381/28/9/094013
- Hobbs, G. B., Edwards, R. T., & Manchester, R. N. 2006, *MNRAS*, 369, 655. doi:10.1111/j.1365-2966.2006.10302.x
- Hobbs, G., Archibald, A., Arzumianian, Z., et al. 2010, *Classical and Quantum Gravity*, 27, 084013. doi:10.1088/0264-9381/27/8/084013
- Hobbs, G., Lyne, A. G., & Kramer, M. 2010, *MNRAS*, 402, 1027. doi:10.1111/j.1365-2966.2009.15938.x
- Hobbs, G. 2013, *Classical and Quantum Gravity*, 30, 224007. doi:10.1088/0264-9381/30/22/224007
- Hobbs, G. & Dai, S. 2017, [arXiv:1707.01615](https://arxiv.org/abs/1707.01615)
- Huang, S.-J., Hu, Y.-M., Korol, V., et al. 2020, [arXiv:2005.07889](https://arxiv.org/abs/2005.07889)
- Hughes, S. A., Warburton, N., Khanna, G., et al. 2021, [arXiv:2102.02713](https://arxiv.org/abs/2102.02713)
- Inayoshi, K., Visbal, E., & Haiman, Z. 2020, *ARA&A*, 58, 27. doi:10.1146/annurev-astro-120419-014455

- Janssen, G., Hobbs, G., McLaughlin, M., et al. 2015, *Advancing Astrophysics with the Square Kilometre Array (AASKA14)*, 37
- Jenet, F. A., Lommen, A., Larson, S. L., et al. 2004, *ApJ*, 606, 799. doi:10.1086/383020
- Jenet, F. A., Hobbs, G. B., Lee, K. J., et al. 2005, *ApJ*, 625, L123. doi:10.1086/431220
- Kagra Collaboration, Akutsu, T., Ando, M., et al. 2019, *Nature Astronomy*, 3, 35. doi:10.1038/s41550-018-0658-y
- Kawamura, S., Nakamura, T., Ando, M., et al. 2006, *Classical and Quantum Gravity*, 23, S125. doi:10.1088/0264-9381/23/8/S17
- Kiziltan, B., Kottas, A., De Yoreo, M., et al. 2013, *ApJ*, 778, 66. doi:10.1088/0004-637X/778/1/66
- Klein, A., Barausse, E., Sesana, A., et al. 2016, *Phys. Rev. D*, 93, 024003
- Kormendy, J. & Ho, L. C. 2013, *ARA&A*, 51, 511. doi:10.1146/annurev-astro-082708-101811
- Korol, V., Rossi, E. M., Groot, P. J., et al. 2017, *MNRAS*, 470, 1894
- Kovetz, E. D., Cholis, I., Breysse, P. C., et al. 2017, *Phys. Rev. D*, 95, 103010. doi:10.1103/PhysRevD.95.103010
- Kramer, M. & Champion, D. J. 2013, *Classical and Quantum Gravity*, 30, 224009. doi:10.1088/0264-9381/30/22/224009
- Kupfer, T., Korol, V., Shah, S., et al. 2018, *MNRAS*, 480, 302. doi:10.1093/mnras/sty1545
- Lamberts, A., Garrison-Kimmel, S., Hopkins, P. F., et al. 2018, *MNRAS*, 480, 2704. doi:10.1093/mnras/sty2035
- Lamberts, A., Blunt, S., Littenberg, T. B., et al. 2019, *MNRAS*, 490, 5888. doi:10.1093/mnras/stz2834
- Lasky, P. D., Mingarelli, C. M. F., Smith, T. L., et al. 2016, *Physical Review X*, 6, 011035. doi:10.1103/PhysRevX.6.011035
- Lau, M. Y. M., Mandel, I., Vigna-Gómez, A., et al. 2020, *MNRAS*, 492, 3061. doi:10.1093/mnras/staa002
- Lentati, L., Taylor, S. R., Mingarelli, C. M. F., et al. 2015, *MNRAS*, 453, 2576. doi:10.1093/mnras/stv1538
- Linde, A. D. 1982, *Physics Letters B*, 108, 389. doi:10.1016/0370-2693(82)91219-9
- Lipunov, V. M., Postnov, K. A., & Prokhorov, M. E. 1997, *New A*, 2, 43. doi:10.1016/S1384-1076(97)00007-9
- London, L., Khan, S., Fauchon-Jones, E., et al. 2018, *Phys. Rev. Lett.*, 120, 161102. doi:10.1103/PhysRevLett.120.161102
- Luo, J., Chen, L.-S., Duan, H.-Z., et al. 2016, *Classical and Quantum Gravity*, 33, 035010. doi:10.1088/0264-9381/33/3/035010
- Madau, P., & Dickinson, M. 2014, *ARA&A*, 52, 415
- Maggiore, M. *Gravitational Waves: Volume 1: Theory and Experiments*. (OUP Oxford, 2008)
- Maggiore, M., Van Den Broeck, C., Bartolo, N., et al. 2020, *J. Cosmology Astropart. Phys.*, 2020, 050. doi:10.1088/1475-7516/2020/03/050
- Magorrian, J., Tremaine, S., Richstone, D., et al. 1998, *AJ*, 115, 2285. doi:10.1086/300353
- Mapelli, M., Giacobbo, N., Ripamonti, E., et al. 2017, *MNRAS*, 472, 2422. doi:10.1093/mnras/stx2123
- McLaughlin, M. A. 2013, *Classical and Quantum Gravity*, 30, 224008. doi:10.1088/0264-9381/30/22/224008
- McWilliams, S. T., Ostriker, J. P., & Pretorius, F. 2014, *ApJ*, 789, 156. doi:10.1088/0004-637X/789/2/156
- McWilliams, S. T., Caldwell, R., Holley-Bockelmann, K., et al. 2019, [arXiv:1903.04592](https://arxiv.org/abs/1903.04592)
- Mei, J., Bai, Y.-Z., Bao, J., et al. 2020, [arXiv:2008.10332](https://arxiv.org/abs/2008.10332)
- Mehta, A. K., Mishra, C. K., Varma, V., et al. 2017, *Phys. Rev. D*, 96, 124010. doi:10.1103/PhysRevD.96.124010
- Miller, M. C. & Miller, J. M. 2015, *Phys. Rep.*, 548, 1. doi:10.1016/j.physrep.2014.09.003
- Mills, C. & Fairhurst, S. 2021, *Phys. Rev. D*, 103, 024042. doi:10.1103/PhysRevD.103.024042
- Moe, M. & Di Stefano, R. 2017, *ApJS*, 230, 15. doi:10.3847/1538-4365/aa6fb6
- Murray, I., Adams, R. P., MacKay, D. J. C., , *Proceedings of the Thirteenth International Conference on Artificial Intelligence and Statistics*, PMLR 9:541-548
- Neal, R.M. 1999, *Bayesian Statistics*, 6, 475
- Nelemans, G. 2018, [arXiv:1807.01060](https://arxiv.org/abs/1807.01060)
- Nelemans, G., Yungelson, L. R., & Portegies Zwart, S. F. 2001, *A&A*, 375, 890. doi:10.1051/0004-6361/20010683
- Nissanke, S., Vallisneri, M., Nelemans, G., et al. 2012, *ApJ*, 758, 131. doi:10.1088/0004-637X/758/2/131
- Ölmez, S., Mandic, V., & Siemens, X. 2010, *Phys. Rev. D*, 81, 104028. doi:10.1103/PhysRevD.81.104028
- Ott, C. D. 2009, *Classical and Quantum Gravity*, 26, 204015. doi:10.1088/0264-9381/26/20/204015
- Özel, F., Psaltis, D., Narayan, R., et al. 2012, *ApJ*, 757, 55. doi:10.1088/0004-637X/757/1/55
- Petiteau, A., Babak, S., Sesana, A., et al. 2013, *Phys. Rev. D*, 87, 064036. doi:10.1103/PhysRevD.87.064036
- Phinney, E. S. 1991, *ApJ*, 380, L17. doi:10.1086/186163
- Phinney, E. S. 2001, [astro-ph/0108028](https://arxiv.org/abs/astro-ph/0108028)
- Pian, E., D'Avanzo, P., Benetti, S., et al. 2017, *Nature*, 551, 67. doi:10.1038/nature24298
- Planck Collaboration, Adam, R., Ade, P. A. R., et al. 2016, *A&A*, 594, A1. doi:10.1051/0004-6361/201527101
- Porayko, N. K., Noutsos, A., Tiburzi, C., et al. 2019, *MNRAS*, 483, 4100. doi:10.1093/mnras/sty3324
- Portegies Zwart, S. F. & McMillan, S. L. W. 2000, *ApJ*, 528, L17. doi:10.1086/312422
- Postnov, K. A. & Yungelson, L. R. 2014, *Living Reviews in Relativity*, 17, 3. doi:10.12942/lrr-2014-3
- Postnov, K. A. & Kuranov, A. G. 2019, *MNRAS*, 483, 3288. doi:10.1093/mnras/sty3313
- Punturo, M., Abernathy, M., Acernese, F., et al. 2010, *Classical and Quantum Gravity*, 27, 194002. doi:10.1088/0264-9381/27/19/194002
- Regimbau, T., Dent, T., Del Pozzo, W., et al. 2012, *Phys. Rev. D*, 86, 122001. doi:10.1103/PhysRevD.86.122001
- Reitze, D., Adhikari, R. X., Ballmer, S., et al. 2019, *BAAS*
- Robson, T., Cornish, N. J., & Liu, C. 2019, *Classical and Quantum Gravity*, 36, 105011. doi:10.1088/1361-6382/ab1101
- Rodriguez, C. L., Farr, B., Farr, W. M., et al. 2013, *Phys. Rev. D*, 88, 084013. doi:10.1103/PhysRevD.88.084013
- Ruiter, A. J., Belczynski, K., Benacquista, M., et al. 2010, *ApJ*, 717, 1006. doi:10.1088/0004-637X/717/2/1006
- Sathyaprakash, B. S. & Schutz, B. F. 2009, *Living Reviews in Relativity*, 12, 2. doi:10.12942/lrr-2009-2
- Sazhin, M. V. 1978, *Soviet Ast.*, 22, 36
- Sesana, A. 2016, *Phys. Rev. Lett.*, 116, 231102. doi:10.1103/PhysRevLett.116.231102
- Sesana, A., Haardt, F., Madau, P., et al. 2005, *ApJ*, 623, 23. doi:10.1086/428492
- Sesana, A., Vecchio, A., & Colacino, C. N. 2008, *MNRAS*, 390, 192. doi:10.1111/j.1365-2966.2008.13682.x
- Sesana, A. & Vecchio, A. 2010, *Phys. Rev. D*, 81, 104008. doi:10.1103/PhysRevD.81.104008
- Sesana, A., Lamberts, A., & Petiteau, A. 2020, *MNRAS*, 494, L75. doi:10.1093/mnras/slaa039
- Schneider, R., Ferrari, V., Matarrese, S., et al. 2001, *MNRAS*, 324, 797. doi:10.1046/j.1365-8711.2001.04217.x
- Schutz, B. F. 1989, *Classical and Quantum Gravity*, 6, 1761. doi:10.1088/0264-9381/6/12/006
- Schutz, K. & Ma, C.-P. 2016, *MNRAS*, 459, 1737. doi:10.1093/mnras/stw768
- Shannon, R. M., Ravi, V., Coles, W. A., et al. 2013, *Science*, 342, 334. doi:10.1126/science.1238012
- Shannon, R. M., Ravi, V., Lentati, L. T., et al. 2015, *Science*, 349, 1522. doi:10.1126/science.aab1910
- Siemens, X., Creighton, J., Maor, I., et al. 2006, *Phys. Rev. D*, 73, 105001. doi:10.1103/PhysRevD.73.105001
- Siemens, X., Mandic, V., & Creighton, J. 2007, *Phys. Rev. Lett.*, 98, 111101. doi:10.1103/PhysRevLett.98.111101
- Starobinsky, A. A. 1980, *Physics Letters B*, 91, 99. doi:10.1016/0370-2693(80)90670-X
- Talbot, C. & Thrane, E. 2018, *ApJ*, 856, 173. doi:10.3847/1538-4357/aab34c
- Tauris, T. M. 2018, *Phys. Rev. Lett.*, 121, 131105. doi:10.1103/PhysRevLett.121.131105
- Timpano, S. E., Rubbo, L. J., & Cornish, N. J. 2006, *Phys. Rev. D*, 73, 122001. doi:10.1103/PhysRevD.73.122001
- Tinto, M. & Armstrong, J. W. 1999, *Phys. Rev. D*, 59, 102003
- LIGO Scientific Collaboration, Aasi, J., Abbott, B. P., et al. 2015, *Classical and Quantum Gravity*, 32, 074001. doi:10.1088/0264-9381/32/7/074001
- The LIGO Scientific Collaboration, the Virgo Collaboration, Abbott, R., et al. 2020, [arXiv:2010.14533](https://arxiv.org/abs/2010.14533)
- Thorne, K. S. 1980, *Reviews of Modern Physics*, 52, 299. doi:10.1103/RevModPhys.52.299
- Thorne, K. S. 1987, *Three Hundred Years of Gravitation*, 330
- Toonen, S., Nelemans, G., & Portegies Zwart, S. 2012, *A&A*, 546, A70. doi:10.1051/0004-6361/201218966
- van Haasteren, R., Levin, Y., McDonald, P., et al. 2009, *MNRAS*, 395, 1005. doi:10.1111/j.1365-2966.2009.14590.x
- van Haasteren, R., Levin, Y., Janssen, G. H., et al. 2011, *MNRAS*, 414, 3117. doi:10.1111/j.1365-2966.2011.18613.x
- Vitale, S. & Evans, M. 2017, *Phys. Rev. D*, 95, 064052. doi:10.1103/PhysRevD.95.064052
- Vitale, S., Farr, W. M., Ng, K. K. Y., et al. 2019, *ApJ*, 886, L1
- Yardley, D. R. B., Hobbs, G. B., Jenet, F. A., et al. 2010, *MNRAS*, 407, 669. doi:10.1111/j.1365-2966.2010.16949.x

- Valentim, R., Rangel, E., & Horvath, J. E. 2011, MNRAS, 414, 1427.
doi:10.1111/j.1365-2966.2011.18477.x
- Vallisneri, M. 2008, Phys. Rev. D, 77, 042001.
doi:10.1103/PhysRevD.77.042001
- Veitch, J., Raymond, V., Farr, B., et al. 2015, Phys. Rev. D, 91, 042003.
doi:10.1103/PhysRevD.91.042003
- Verbiest, J. P. W., Lentati, L., Hobbs, G., et al. 2016, MNRAS, 458, 1267.
doi:10.1093/mnras/stw347
- Yi, S., Stappers, B. W., Sanidas, S. A., et al. 2014, MNRAS, 445, 1245.
doi:10.1093/mnras/stu1826
- Yu, S. & Jeffery, C. S. 2010, A&A, 521, A85. doi:10.1051/0004-6361/201014827
- Zhang, J., Yang, Y., Zhang, C., et al. 2019, MNRAS, 488, 5020.
doi:10.1093/mnras/stz2020

Appendix A: Conversion among different LISA responses

In above sections, when working with LISA responses to gravitational wave signal and noises, we often need to convert among different kinds of LISA responses. We summarise the conversion relationship in figure A.1.

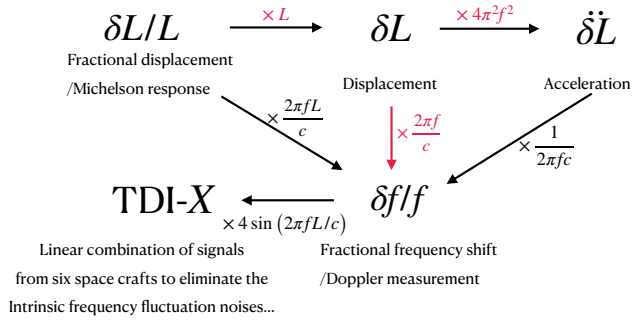


Fig. A.1. Conversion between different kinds of LISA responses